Quarterly Report for

Contract DE-FG36-08GO18192

Stanford Geothermal Program

July-September 2010

Table of Contents

1. FRACTURE CHARACTERIZATION USING PRODUCTION DATA

This research project is being conducted by Research Assistant Egill Juliusson, Senior Research Engineer Kewen Li and Professor Roland Horne. The objective of this project is to investigate ways to characterize fractures in geothermal reservoirs using production data.

1.1 SUMMARY

The quarter's activities in this project are reported in three parts. The first part is on advances that have been made in solving the advection-dispersion equation which governs tracer and thermal transport. The key idea behind these advances is to encode the tracer production in terms of cumulative injection, as opposed to time. This way to tracer production can be computed for any given flow rate. Moreover, these advances can be used in the two-dimensional discrete fracture network simulator, discussed in earlier quarterly reports (winter and spring 2010).

The second part is a review of methods that have been identified for the interpretation of pressure or flow rate communication between wells. The section is divided into subsections on rate-pressure, pressure-pressure and rate-rate regression models. The rate-rate regression models are covered more extensively than the others, since these methods look promising for prediction of flow rates in enhanced geothermal systems.

Finally, we document the various types of regression models that have been used to infer well-to-well connectivity in this investigation. The discussion helps clarify the linkage between the various linear and nonlinear, and parametric or nonparametric approaches that have been suggested. The simplest and most restrictive methods are reviewed first, and the discussion ends with a review of the alternating conditional expectation model, which is very flexible, but has relatively poor predictive power.

1.2 INTRODUCTION

A part of this project has focused on the numerical simulation of tracer transport through fractures. Traditional finite volume and finite element simulators have not proven to be very efficient in handling such simulations because of computational inefficiencies that arise due the interplay between fast traveling tracer fronts, small computational elements and time stepping.

In the quarterly reports from winter and spring 2010 a fast but simplified numerical modeling method for calculating flow through a discrete fracture network was discussed. The method was developed based on the assumption of steady-state, incompressible single-phase flow, which made the problem analogous to analyzing a network of resistors. The single-phase incompressibility assumption should be a good approximation for most EGS (Enhanced Geothermal Systems) and other single-phase geothermal systems. The effects and implementation of Taylor dispersion were also discussed, and in particular the sensitivity of the solution to how fractures are modeled.

In this quarterly report, a solution to the one-dimensional advection-dispersion equation for transient flow rate and dispersion is developed. This solution may be of interest on its own, since it is a general and compact analytical solution to a commonly encountered partial differential equation, which has not been reported in the literature to the best of our knowledge. The key idea is to transform the time variable into cumulative injection. Although it has not yet been verified it looks like this transformation is applicable to many known solutions of the advection-dispersion equation, even in two or three dimensions. Moreover, this solution brings the possibility of lifting the steady-state flow condition on the discrete fracture simulator discussed in the previous paragraph

Much of our work to date has focused on tracer transport. To broaden the horizon we have looked into pressure and flow rate data. A brief literature survey of methods for interpreting pressure and rate signals between wells is presented here. This field seems to be addressed well by researchers in the petroleum industry and a couple of promising methods were identified. Some of the key components of the methods were also implemented to enhance our understanding of how they work.

Several regression methods have been used in this project and related projects to infer well-to-well connectivity using tracer data. These methods have evolved in complexity in an attempt to capture the rather complex pattern of tracer returns under variable injection conditions. It is worthwhile to review these methods, along with the main assumptions made to allow greater flexibility in capturing complex time series. This shows also that care must be taken in choosing not too complex a model, since that can lead to models with poor predictive capacity.

1.3 ADVECTION-DISPERSION EQUATION WITH TIME VARYING COEFFICIENTS

A key element for the extension of the discrete fracture simulator discussed in the quarterly reports from winter and spring 2010 was to develop an analytical solution for tracer transport under transient flow conditions (transient flow rate and dispersion). In this case, the advection dispersion equation would be:

$$\frac{\partial c}{\partial t} + u(t)\frac{\partial c}{\partial x} - D(t)\frac{\partial^2 c}{\partial t^2} = 0 \qquad (2.1)$$

Here we will show the development of a solution to this equation, using the known solution for the impulse response on an infinite x-domain, assuming constant velocity, u_0, and dispersivity, D_0. This solution, for a tracer slug (impulse) of mass m released at $x = 0$, at time t_0 is:

$$c(x,t|t_0,u_0,D_0) = \frac{m}{A\sqrt{4\pi D_0(t-t_0)}}\, e^{-\frac{(u_0(t-t_0)-x)^2}{4D_0(t-t_0)}} \quad t > t_0 \qquad (2.2)$$

This essentially describes a normal distribution in x, with a linearly increasing mean, $u_0(t-t_0)$, and variance, $2D_0(t-t_0)$. The state of the tracer concentration as a function of x at a time t_1 is shown in Figure 1.1, along with the observed concentration at a location ξ, at times $t_0 < t < t_1$.

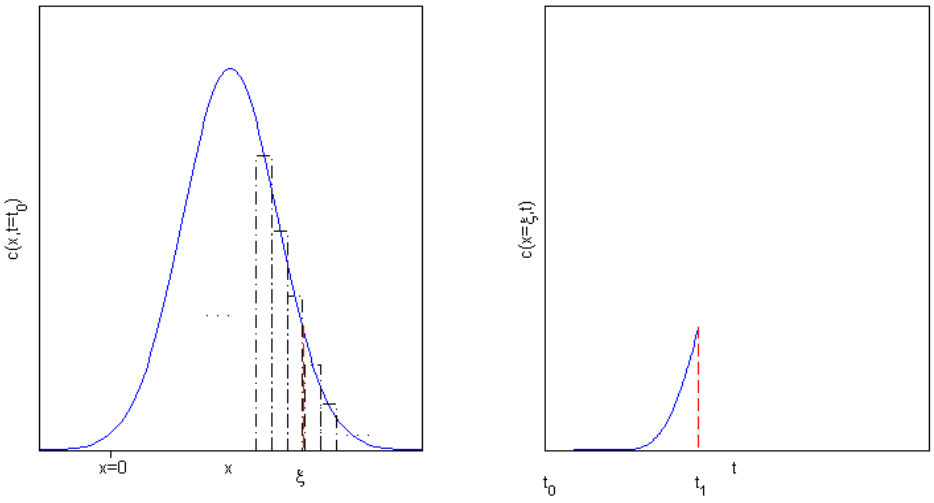

Figure 1.1: Tracer slug as a function of x (on the left) and as seen at location ξ, up until time t_1.

Now, say that at time, t_1, the injection rate changes such that the flow velocity and dispersion become u_1 and D_1. The observed returns at ξ after t_1 can be computed by identifying that the response at ξ is a combination of impulse responses coming from small impulses released at incremental locations along x (dashed boxes in Figure 1.1), each with associated mass:

$$dm(x,t_1) = c(x,t_1|t_0,u_0,D_0)Adx = \frac{m\,dx}{\sqrt{4\pi D_0(t_1-t_0)}}e^{-\frac{(u_0(t_1-t_0)-x)^2}{4D_0(t_1-t_0)}} \qquad (2.3)$$

Thus, the concentration function becomes:

$$c\big(x,t|t_0,u_0,D_0,t_1,u_1,D_1\big) = \begin{cases} c(x,t|t_0,u_0,D_0) & t_0 < t < t_1 \\ \int_{-\infty}^{\infty} \frac{c(x-\xi,t|t_1,u_1,D_1)}{m}\,dm(\xi,t_1) & t_1 > t \end{cases} \qquad (2.4)$$

or:

$$c\big(x,t|t_0,u_0,D_0,t_1,u_1,D_1\big) = \begin{cases} c(x,t|t_0,u_0,D_0) & t_0 < t < t_1 \\ \dfrac{A}{m}\displaystyle\int_{-\infty}^{\infty} c(x-\xi,t|t_1,u_1,D_1)c(\xi,t_1|t_0,u_0,D_0)\,d\xi & t_1 > t \end{cases} \tag{2.5}$$

Note here that after time t_1 we have a convolution of two impulse responses, in terms of x. Remembering that the impulse response can be viewed as a normal probability distribution, scaled by m/A, we obtain:

$$\begin{aligned} c(x,t|t_0,u_0,D_0) &= \frac{m}{A}\frac{1}{\sqrt{4\pi D_0(t-t_0)}}e^{-\frac{(u_0(t-t_0)-x)^2}{4D_0(t-t_0)}} \\ &= \frac{m}{A}f_{\mathcal{N}}(x|u_0(t-t_0),2D_0(t-t_0)) \quad t > t_0 \end{aligned} \tag{2.6}$$

where $f_{\mathcal{N}}(x|u_0(t-t_0),2D_0(t-t_0))$ denotes the probability density function (pdf) for a normally distributed variable with mean $u_0(t-t_0)$ and variance $2D_0(t-t_0)$. The first key observation here is that the sum, Y, of two normally distributed random variables, say X_1 and X_2, will have a mean equal to the sum of the means of X_1 and X_2. Similarly the variance of Y will be the sum of the variances of X_1 and X_2. Secondly it is important to observe, that the pdf of Y, is the convolution of the pdf's of X_1 and X_2, which is precisely what was seen in (2.5). Thus,

$$\begin{aligned} &c\big(x,t|t_0,u_0,D_0,t_1,u_1,D_1\big) \\ &= \begin{cases} c(x,t|t_0,u_0,D_0) & t_0 < t < t_1 \\ \dfrac{m}{A}\displaystyle\int_{-\infty}^{\infty} f_{\mathcal{N}}(x-\xi|u_1(t-t_1),2D_1(t-t_1))f_{\mathcal{N}}\big(\xi\big|u_0(t_1-t_0),2D_0(t_1-t_0)\big)\,d\xi & t_1 > t \end{cases} \\ &= \begin{cases} \dfrac{m}{A}f_{\mathcal{N}}\big(x\big|u_0(t-t_0),2D_0(t-t_0)\big) & t_0 < t < t_1 \\ \dfrac{m}{A}f_{\mathcal{N}}(x|u_0(t_1-t_0)+u_1(t-t_1),2D_0(t_1-t_0)+2D_1(t-t_1)) & t_1 > t \end{cases} \end{aligned} \tag{2.7}$$

From this point it is straight forward to infer that if the flow rate is changed again, with a corresponding change in u and D, these changes can be incorporated into the mean and variance of $f_{\mathcal{N}}$. For example after k changes in injection:

$$\begin{aligned} &c\big(x,t|t_0,u_0,D_{0,}\dots,t_k,u_k,D_k\big) \\ &= \frac{m}{A}f_{\mathcal{N}}\big(x\big|u_0(t_1-t_0)+\cdots+u_k(t-t_k),2D_0(t_1-t_0)+\cdots+2D_k(t-t_k)\big) \quad t_k > \end{aligned} \tag{2.8}$$

Letting the changes in time, $\Delta t = t_{i+1} - t_i$, become incrementally small leads to the solution of (2.1), given a tracer slug of mass m released at $x = 0$, at time t_0:

$$\begin{aligned} c(x,t|u(t),D(t)) &= \frac{m}{A} f_{\mathcal{N}}\left(x \middle| \int_{t_0}^{t} u(\tau)d\tau, 2\int_{t_0}^{t} D(\tau)d\tau\right) \quad u(t),D(t) \geq 0 \\ &= \frac{m}{A\sqrt{4\pi \int_{t_0}^{t} D(\tau)d\tau}} e^{-\frac{\left(\int_{t_0}^{t} u(\tau)d\tau - x\right)^2}{4\int_{t_0}^{t} D(\tau)d\tau}} \quad u(t),D(t) \geq 0 \end{aligned} \tag{2.9}$$

A discrete (albeit slightly convoluted) version of this formulation was derived by Carlier (2008). Carlier also listed three other impulse response solutions, derived for different boundary conditions. The solution given for a constant flux concentration boundary on a semiinfinite domain for constant u and D is (Zuber, 1974):

$$c(x,t|t_0,u_0,D_0) = \frac{mx}{Au_0(t-t_0)\sqrt{4\pi D_0(t-t_0)}} e^{-\frac{(u_0(t-t_0)-x)^2}{4D_0(t-t_0)}} \quad t > t_0, x > 0 \tag{2.10}$$

Carlier generalized this solution for a discrete number of flow periods. If we let these discrete periods become incrementally small the solution generalizes to an expression similar to Equation (2.9):

$$\begin{aligned} &c(x,t|u(t),D(t)) \\ &= \frac{mx}{A\int_{t_0}^{t} u(\tau)d\tau \sqrt{4\pi \int_{t_0}^{t} D(\tau)d\tau}} e^{-\frac{\left(\int_{t_0}^{t} u(\tau)d\tau - x\right)^2}{4\int_{t_0}^{t} D(\tau)d\tau}} \quad u(t),D(t),x \geq 0 \end{aligned} \tag{2.11}$$

Here it has been shown that two impulse response solutions which were derived for constant u and D, can be generalized to solutions with time varying coefficients by replacing ut with $\int_{t_0}^{t} u(\tau)d\tau$ and Dt with $\int_{t_0}^{t} D(\tau)d\tau$. It seems logical to suppose that other versions of impulse response solutions to the advection dispersion equation could be generalized in the same manner, e.g. Equations (7), (8), (26) and (27) in Carlier (2008).

Figure 1.2 shows the semiinfinite and infinite impulse responses to a sinusoidal flow rate and a step-wise varying flow rate (in this case we let $q(t) = u(t) = D(t)$).

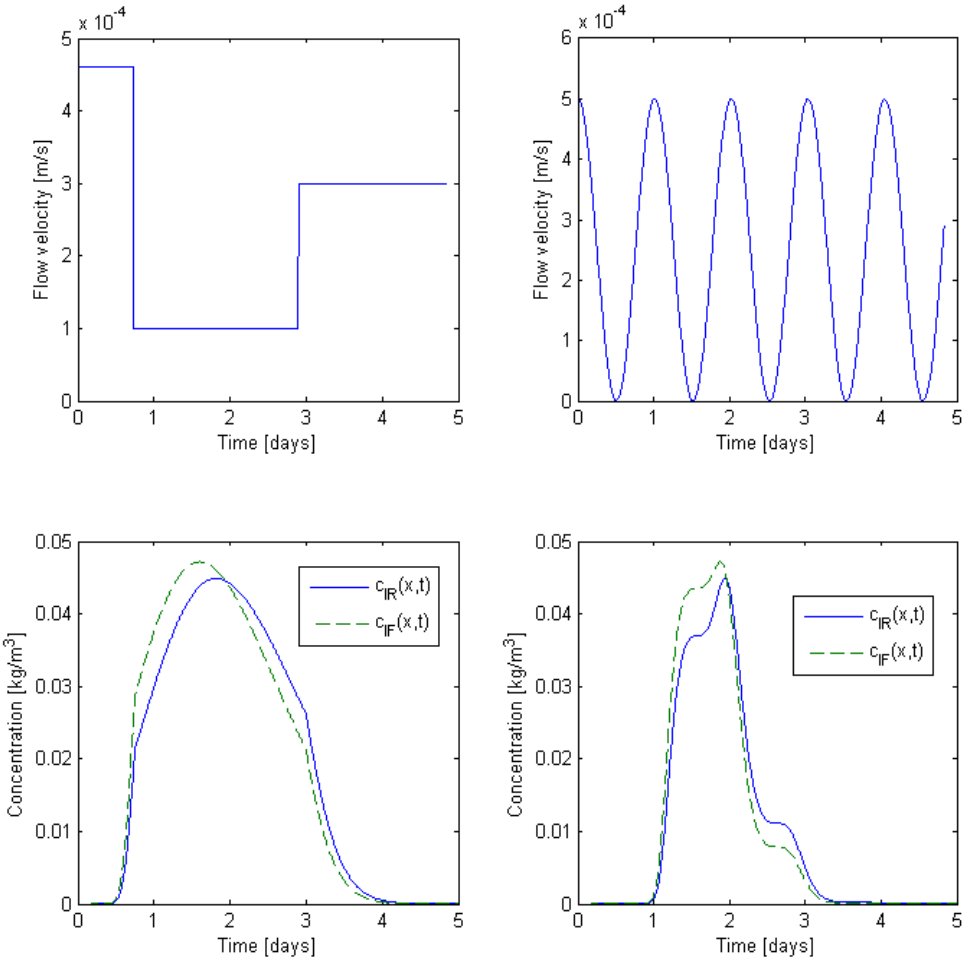

Figure 1.2: Impulse responses to the advection-dispersion equation with varying flow velocity and dispersion. The time varying flow velocities are above the corresponding impulse responses for an infinite medium (c_{IR}) and a semiinfinite medium (c_{IF}). Here $m = 1kg,\ A = 1m^2, x = 40m$, and $D(t) = u(t)$.

The impulse response can be used to find the response for any transient input of the tracer concentration. To see this, imagine a series of impulses, released from point $x = 0$ at times t'. Each impulse has mass:

$$dm(t') = c(x = 0, t')u(t')Adt' = c_0(t')u(t')Adt' \tag{2.12}$$

where $c_0(t)$ is a time varying concentration introduced to the flow stream at $x = 0$. Replacing m in (2.9) with $dm(t')$, and integrating with respect to t' over all times from 0 to t, leads to the concentration for any time varying concentration injected.

$$c(x,t|u(t),D(t),c_0(t)) = \int_0^t \frac{dm(t')}{A\sqrt{4\pi\int_{t'}^t D(\tau)d\tau}} e^{-\frac{\left(\int_{t'}^t u(\tau)d\tau - x\right)^2}{4\int_{t'}^t D(\tau)d\tau}} = \int_0^t \frac{c_0(t')u(t')}{\sqrt{4\pi\int_{t'}^t D(\tau)d\tau}} e^{-\frac{\left(\int_{t'}^t u(\tau)d\tau - x\right)^2}{4\int_{t'}^t D(\tau)d\tau}} dt' \quad (2.13)$$

Similarly, for the semiinfinite case, replacing m in Equation (2.11) with $dm(t')$ leads to:

$$c(x,t|u(t),D(t),c_0(t)) = \int_0^t \frac{c_0(t')u(t')x}{\int_{t'}^t u(\tau)d\tau\sqrt{4\pi\int_{t'}^t D(\tau)d\tau}} e^{-\frac{\left(\int_{t'}^t u(\tau)d\tau - x\right)^2}{4\int_{t'}^t D(\tau)d\tau}} dt' \quad (2.14)$$

Tracer responses for the same situation as presented in Figure 1.2, except with a linearly increasing concentration, are shown in Figure 1.3.

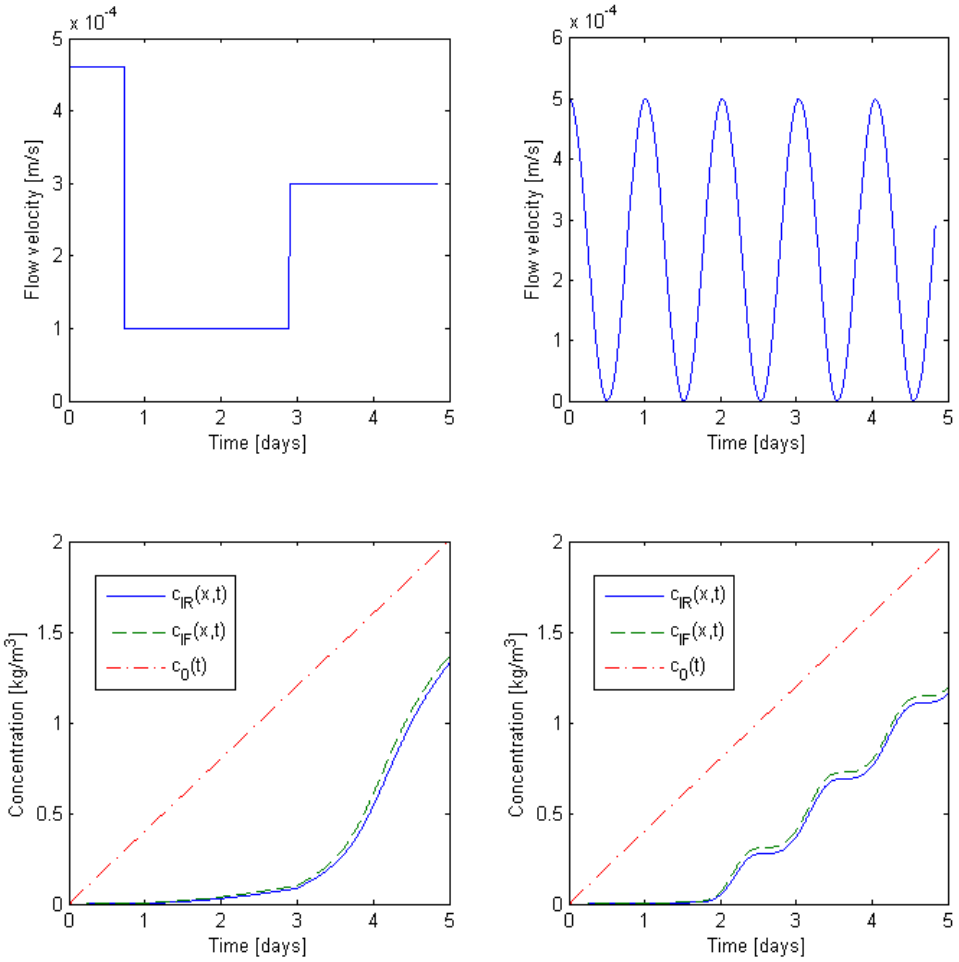

Figure 1.3: Responses to the advection-dispersion equation with a linearly increasing injection concentration (c_0) and varying flow velocity and dispersion. The time varying flow velocities, $u(t)$, are above the corresponding responses for an infinite medium (c_{IR}) and a semiinfinite medium (c_{IF}). Here $m = 1kg$, $A = 1m^2$, $x = 40m$, and $D(t) = u(t)$.

1.3.1 Cumulative injection model for multiwell tracer tests

Although the models presented in Equations (2.13) and (2.14) lack some essential properties, e.g. matrix diffusion (Jensen, 1983), they give some insight into which predictors might be appropriate for finding a unique transfer function between injector and producer. Take Equation (2.13) for example. Assuming that dispersion depends on velocity as $D(t) = \alpha u(t)$ and letting $q(t) = Au(t)$, Equation (2.13) can be rewritten as:

$$c(x,t|q(t),c_0(t)) = \int_0^t \frac{c_0(t')q(t')}{\sqrt{4\pi A\alpha \int_{t'}^t q(\tau)d\tau}} e^{-\frac{\left(\int_{t'}^t q(\tau)d\tau - Ax\right)^2}{4A\alpha \int_{t'}^t q(\tau)d\tau}} dt' \qquad (2.15)$$

Noting that:

$$\int_{t'}^t q(\tau)d\tau = \int_0^t q(\tau)d\tau - \int_0^{t'} q(\tau)d\tau = Q_0(t) - Q_0(t') \qquad (2.16)$$
$$dQ_0(t') = q(t')dt'$$

Substituting into (2.15) gives:

$$c(x,t|Q_0(t),c_0(t)) = \int_0^{Q_0(t)} \frac{c_0\left(Q_0(t')\right)}{\sqrt{4\pi A\alpha(Q_0(t) - Q_0(t'))}} e^{-\frac{(Q_0(t)-Q_0(t')-Ax)^2}{4A\alpha(Q_0(t)-Q_0(t'))}} dQ_0(t') \qquad (2.17)$$

Equation (2.17) is a convolution equation in terms of cumulative injection. To be able to use it the concentration needs to be represented as a function of cumulative injection, and the transfer function will also be a function of cumulative injection. This transfer function, however, is representative of the connectivity between the wells, independent of what the current injection rate is. Therefore, it can be applied to predict tracer breakthrough at any injection rate, and it can be compared to other such transfer functions without the bias caused by variable injection rates. Moreover, this type of model might work well in conjunction with a pressure or rate based model, since the signals generated by varying both injection rate and concentration at the same time could be interpreted by these methods. For example, a nonparametric deconvolution approach, similar to that introduced in the quarterly report from summer 2009 would probably work well.

1.4 INTERPRETATION METHODS FOR PRESSURE AND FLOW RATE DATA

The interpretation of pressure signals has been a long standing research topic in both the ground water hydrology and the petroleum sciences. A multitude of regression methods, analytical models and numerical models have been documented. This section provides a brief overview of a few notable methods, relating rate-pressure, pressure-pressure and rate-rate interactions between wells. Nonparametric models based on the pressure equation, will in generally involve solutions of the deconvolution problem, because pressure disturbances in the reservoir are superposable. The pressure and rate in a well are often linearly related, which makes it possible to find a unique transfer function between pressure, or rate, in one well and pressure, or rate, in another well.

1.4.1 Rate-pressure models

Rate-pressure transfer functions are commonly used in well tests and interference tests. A multitude of analytical solutions for these types of models are in the literature, some of which are given in Lee (1982). Some very interesting generalizations of the analytical well test models for fractal dimensions can be found in the paper by Barker (1988).

If an analytical rate-pressure model is not assumed, one can still assert (based on the superposition principle) that a change in production rate at $\boldsymbol{x} = 0$ will induce a pressure change at $\boldsymbol{x}$ according to the convolution equation:

$$p(\boldsymbol{x}, t) = p_0(\boldsymbol{x}) - \int_0^t q(\boldsymbol{0}, t-\tau) g(\boldsymbol{x}, \tau) d\tau \tag{2.18}$$

Discusssions of the validity of this assumption can be found in Deng and Horne (1993) and Schroeter and Gringarten (2007), which conclude that if wellbore storage and skin effect are negligible, it should hold (and in many other cases as well). In other words, if q and p are representative for measurements within the formation, then Equation (2.18) should hold.

The unknown in Equation (2.18) is the pressure impulse response, g, which is the time derivative of the rate normalized pressure, $p_u(\boldsymbol{x}, t)$. This is the characteristic rate-pressure transfer function between the two wells in question, and it is determined by the physics of the reservoir. It is related to the diagnostic pressure derivative in well testing as follows:

$$dp_u(\boldsymbol{x}, t)/dln(t) = t\, dp_u(\boldsymbol{x}, t)/dt = tg(\boldsymbol{x}, t) \tag{2.19}$$

Schroeter et al. (2004) developed a widely used nonparametric single well deconvolution method for simultaneously obtaining $tg(\boldsymbol{x}, t)$ and $q(\boldsymbol{0}, t)$. Some aspects of this method were improved by Levitan (2005) and Pimonov et al. (2009), but the basic method in the 2004 publication is still the industry standard. The crux of the method is to transform the problem to a logarithmic time scale. This makes the problem nonlinear, which is not good, but it also makes it easier to capture the important part pressure transient with relatively few unknown parameters. A number of other deconvolution methods have also been proposed e.g. by Nomura and Horne (2009) and many others which are referred to in Schroeter et al (2004).

Levitan (2006) also extended the work of Schroeter et al. (2004) to include the effects of multiple wells. The multiwell deconvolution equation is:

$$p(\boldsymbol{x_i}, t) = p_0(\boldsymbol{x_i}) - \sum_{j=1}^{N_w} \int_0^t q\big(\boldsymbol{x_j}, t-\tau\big) g\big(\Delta \boldsymbol{x_{ij}}, \tau\big) d\tau \tag{2.20}$$

where i and j refer to each of the N_w wells in the reservoir. Levitan (2006) asserts that only pressure build-up data can be used for the deconvolution method, because variable skin effects often seen between drawdown and build-up would violate the deconvolution principle. He also stresses that it is impractical to extract information about the interwell transfer functions between wells i and j when both wells are active. The reason is that the pressure signal from the active well on itself (p_{ii}) will overshadow the interwell pressure signal (p_{ij}). Finally he mentions that the multiwell rate-pressure convolution problem could benefit from work on optimal production-injection signals, that would provide transients that are well suited for deconvolution.

It is clear from this summary that researchers of well-to-well interaction in terms of rate-pressure data have worked on problems similar to those that have been found for well-to-well tracer interactions in this research project. Schroeter et al. (2004) solved the problem of finding an appropriate time scale by a logarithmic transformation of the time scales. In the quarterly report from summer 2009 we faced a similar problem of time scales that were hard to quantify, which was solved using a set of heuristic search algorithms. In the first section of this report we are suggesting a transformation of the time variable into cumulative injection. Finally, we also dealt with the problem of designing injection schedules that provide highly informative tracer transients, which is similar to the pressure transient topic mentioned by Levitan (2006).

To highlight some of the differences between the pressure and tracer problem, we note that the pressure transport is governed by the diffusion equation, and the response is generally a linear function of the pressure change that caused the disturbance. Moreover, most of the pressure response is usually seen within a very short time frame, as compared to the tracer response. A pressure pulse is usually much easier to send and measure than is a tracer pulse. The tracer response is governed by the advection-dispersion equation. This means the tracer response is a linear function of the injected tracer concentration (which caused the disturbance), but a nonlinear function of the flow rate. Therefore, the well-to-well transfer functions (κ_{ij}) that were found by deconvolution in the summer 2009 quarterly report were specific to a single set of steady-state injection and production rates. This problem might however be solved by viewing the transfer function in terms of cumulative injection.

1.4.2 Pressure-Pressure models

Pressure-pressure deconvolution studies are less abundant in the literature. In fact we only reviewed a single study of pressure-pressure deconvolution, i.e. that of Onur et al. (2009). The work of Onur et al. utilized the deconvolution algorithm of Schroeter et al. (2004) with the extensions from Pimonov et al. (2009). It is shown that the pressure-pressure relationship can be modeled by the convolution equation:

$$p(\boldsymbol{x}, t) = p_0(\boldsymbol{x}) - \int_0^t p(0, t-\tau) G(\boldsymbol{x}, \tau) d\tau \qquad (2.21)$$

where $G(\boldsymbol{x}, t)$ is the pressure-pressure impulse response that is to be determined. By comparison of Equations (2.21) and (2.18), it is not surprising that the same deconvolution methods are applicable.

Much of the discussion in Onur et al. is on the diagnostic interpretation of tG, which is similar to that of the diagnostic derivative, tg, for rate-pressure responses. The main advantages mentioned for pressure-pressure deconvolution are that pressure signals are often less susceptible to noise and that G is independent of wellbore storage. It is stated that G is a unique function of the skin factor and the hydraulic diffusivity. This also means that problems are encountered in the presence of variable skin, and that permeability and porosity cannot be estimated individually.

1.4.3 Rate-rate models

Rate-rate models seem to have captured the attention of a slightly different group of researchers within the petroleum industry. The methods of characterizing the transfer functions in rate-rate modeling have been less focused on capturing the details of the transients, and more focused on multiwell applications and the long term effects that controlled injection has on production rates. Much work has been done on the so called capacitor-resistor models (CRM), which draw upon an analogy between the well-to-well connections and electric circuitry. Several variations of the CRM model have been suggested, e.g. by Yousef et al. (2005), Sayarpour et al. (2006) and Lee et al. (2009, 2010). The governing differential equation used for the development of the CRM, assuming constant bottomhole pressure at the producer, is:

$$\frac{dq_p(t)}{dt} + \frac{1}{\mathrm{T}} q_p(t) = \frac{1}{\mathrm{T}} q_r(t) \tag{2.22}$$

Here the subscripts p and r refer to production and re-injection, and T is a time constant representative of the drainage volume between the injector and producer. This equation has the solution:

$$q_p(t) = q_p(0) e^{-\frac{t}{\mathrm{T}}} + \int_0^t q_r(t-\tau) \frac{e^{-\frac{\tau}{\mathrm{T}}}}{\mathrm{T}} d\tau \tag{2.23}$$

It is clear by contemplating this solution that the long term production rate will tend to follow the injection rate, and the time lag will be defined by the time constant T. Note also that the second term on the right is a convolution integral, similar to that shown in Equations (2.18) and (2.21). In this case, however, an analytical transfer function is assumed to be known, and only the time constant, T, is what needs to be determined.

A multiwell analog of equation (2.23) was also derived by Yousef et al. (2006) (here assuming constant bottomhole pressure at the producer):

$$q_{p,i}(t) = \lambda_{p,i} q_{p,i}(0) e^{-\frac{t}{\mathrm{T_{p,i}}}} + \sum_{j=1}^{N_r} \int_0^t q_{r,j}(t-\tau) \lambda_{r,ij} \frac{e^{-\frac{\tau}{\mathrm{T_{r,ij}}}}}{\mathrm{T_{r,ij}}} d\tau \qquad (2.24)$$

In this case, the indexes i and j refer to specific producers and injectors, respectively. The factor λ_p should ideally be 1, but was included to allow more flexibility in fitting the model at late times. Note here that given constant injection rates, the late time production rate will be the weighted sum of the injection rates, with $\lambda_{r,ij}$ defining the weights. Thus, $\lambda_{r,ij}$ can be viewed as the long term contribution of injection in injector j to the production in producer i.

The CRM model is essentially a parametric model, where the unknowns are the parameters λ and T. An alternative approach, more in the line with what this research project has focused on, and the work of Schroeter et al. (2004), is to model the transfer function nonparametrically. Since the analytical solution of the rate-rate model is based on the convolution integral, a deconvolution approach is well suited to find the nonparametric transfer function. This approach was carried out by Lee et al. (2009), where he proposed a model of the form:

$$q_{p,i}(t) = q_{p,i}(0) e^{-\frac{t}{\mathrm{T_{p,i}}}} + \sum_{j=1}^{N_r} \int_0^t q_{r,j}(t-\tau) h_{ij}(\tau) d\tau \qquad (2.25)$$

in which h denotes the nonparametric function to be determined. Lee et al. solved this equation using a deconvolution algorithm, similar to the one we proposed in the quarterly report from summer 2009. They did not, however, adjust the time scales dynamically and therefore the estimates for h were rather coarse. We suspect that the main reason for the method working as well as reported is that the test examples were based on data where the flow rates would stabilize quickly and thus the model was mostly being fitted to steady-state data points. This may very well applicable in practice, especially with incompressible (or slightly compressible) flows, where the time constant should be very small.

In Lee et al. (2010) the development of the rate-rate model was based on a set of coupled differential equations similar to Equation (2.22), where for each of the N_p producers there was an equation of the form:

$$\frac{dq_{p,i}(t)}{dt} + \sum_{k=1}^{N_p} \frac{\alpha_{ik}}{\mathrm{T_i}} q_{p,k}(t) = \sum_{j=1}^{N_r} \frac{\beta_{ij}}{\mathrm{T_i}} q_{r,j}(t) \qquad (2.26)$$

This set of equations can be represented in matrix form as:

$$\frac{d\boldsymbol{q_p}(t)}{dt} + A_c\boldsymbol{q_p}(t) = B_c\boldsymbol{q_r}(t) \tag{2.27}$$

where:

$$A_c = \begin{bmatrix} \mathrm{T}_1 & \cdots & 0 \\ \vdots & \ddots & \vdots \\ 0 & \cdots & \mathrm{T}_{N_p} \end{bmatrix}^{-1} \begin{bmatrix} \alpha_{11} & \cdots & \alpha_{1N_p} \\ \vdots & \ddots & \vdots \\ \alpha_{N_p1} & \cdots & \alpha_{N_pN_p} \end{bmatrix} \tag{2.28}$$

and:

$$B_c = \begin{bmatrix} \mathrm{T}_1 & \cdots & 0 \\ \vdots & \ddots & \vdots \\ 0 & \cdots & \mathrm{T}_{N_p} \end{bmatrix}^{-1} \begin{bmatrix} \beta_{11} & \cdots & \beta_{1N_p} \\ \vdots & \ddots & \vdots \\ \beta_{N_r1} & \cdots & \beta_{N_rN_p} \end{bmatrix} \tag{2.29}$$

The solution to (2.27) is quite similar to equations (2.23) and (2.24), i.e.:

$$\boldsymbol{q_p}(t) = \boldsymbol{q_p}(0)e^{-A_ct} + \int_0^t \boldsymbol{q_r}(t-\tau)B_ce^{-A_c\tau}d\tau \tag{2.30}$$

The main additional development in this solution is that the producer-producer interactions are now also taken into account, in addition to the injector-producer interactions. For practical applications it is more convenient to deal with the discrete form of Equation (2.27). This was done by Lee et al. (2010), which presented the discrete counterpart of (2.27) as:

$$\boldsymbol{q_p}(n+1) = -A\boldsymbol{q_p}(n) + B\boldsymbol{q_r}(n) \tag{2.31}$$

where n is a time-like discrete variable, and A and B are the discrete counterparts of A_c and B_c, respectively. Equation (2.31) defines a multivariate autoregressive model for determining $\boldsymbol{q_p}$ with exogenous inputs, $\boldsymbol{q_r}$. It is referred to as the M-ARX model. A set of $N+1$ measurements yields N equations which can be solved together to find the elements of A and B.

$$\left[\boldsymbol{q_p}(2) \ldots \boldsymbol{q_p}(N+1)\right] = [-A+B]\begin{bmatrix} \boldsymbol{q_p}(1) & \ldots & \boldsymbol{q_p}(N) \\ \boldsymbol{q_r}(1) & \ldots & \boldsymbol{q_r}(N) \end{bmatrix} \tag{2.32}$$

To ensure that the solution is stable, it is important to add the constraint that $A \preccurlyeq 1$ (element-wise), or that $(I+A)^{-1}B \preccurlyeq 1$. It can be shown via the z-transform (discrete analog of Laplace transform) that if the injection rates are kept constant, the production will stabilize at:

$$\boldsymbol{q_p} = (I+A)^{-1}B\boldsymbol{q_r} = F\boldsymbol{q_r} \tag{2.33}$$

The matrix $F = (I + A)^{-1}B$ then defines the interwell connectivity for each of the injector-producer pairs in terms of flow rate.

If the total compressibility is small, the flow rates stabilize relatively quickly, i.e. within a few hours. This would likely be the case for production from enhanced geothermal systems, and thus the M-ARX model would be ideal, e.g. for reinjection scheduling.

1.5 SUMMARY OF REGRESSION MODELING METHODS

In this section we give an overview of the regression methods that have been used in this research project to infer interwell connectivity. We will try to keep the equations general in terms of notation, and give examples through references to other papers. In general we will refer to x as the input or predictor variable, and y as the output or response variable. We will also attempt to give graphical representations of each method to enhance understanding and shed light on the similarities and differences between each method.

1.5.1 Multiple input linear regression

Multiple linear regression is a model that relates a linear combination of multiple inputs, x_j, to a single output, y. In most cases there are multiple measurements in time so we have $x(t)$ and $y(t)$.

$$y(t) = \sum_{j=1}^{N_j} a_j x_j\,(t) \tag{2.34}$$

Where N_j is the number of inputs, and the parameters a_j are the unknowns. Since there are usually more time measurements than unknowns, there will be more relations of the type (2.34) than unknowns and the a_j can be uniquely determined. A time lag, τ_j, could also be considered by modifying (2.34) to:

$$y(t) = \sum_{j=1}^{N_j} a_j x_j\left(t - \tau_j\right) \tag{2.35}$$

The slopes, a_j, are generally assumed to be independent and can take any value. The multiple input linear regression model represented by (2.35) is shown graphically in Figure 1.4.

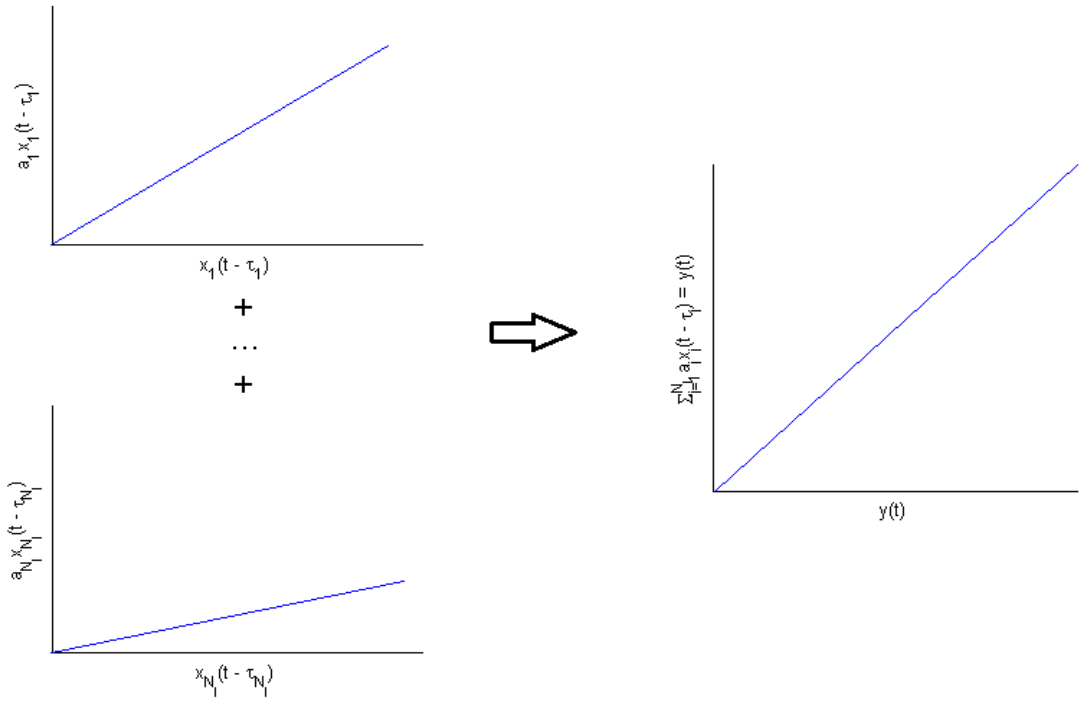

Figure 1.4: Linear regression model with multiple inputs and possible time lags

The work of Urbino and Horne (1991) and Sullera and Horne (2001), relied mostly on regression models of this type, without the inclusion of time lags. The inclusion of time lags was presented earlier in this research project, in the quarterly report for winter 2009. The M-ARX model applied by Lee et al. (2010) can also be seen as a multiple input linear regression model, where some of the inputs, were the same as the output, but with a constant time lag.

1.5.2 Single input convolution

The single input convolution model in continuous form is:

$$y(t) = \int_0^t x(t-\tau) f(\tau) d\tau \tag{2.36}$$

In discrete from this can be written as:

$$y(t_k) = \sum_{i=1}^{n(k)} a_i x(t_k - \tau_i) \tag{2.37}$$

Where k is a counter of time measurements, $n(k)$ denotes a number dependent on k, $a_i = f(\tau_i)\Delta\tau_i$, and $\Delta\tau_i$ is determined by the discretization used to approximate the integral. In equation (2.37) the function f is represented as a series of scalars, rather than a specific function of some undetermined parameters. That is why this is called a nonparametric model. Equation (2.37) clearly defines a linear regression system, much like Equation (2.35). The difference is that in the convolution model there are inputs from only one source, but with multiple time lags. Figure 1.5 shows the convolution model.

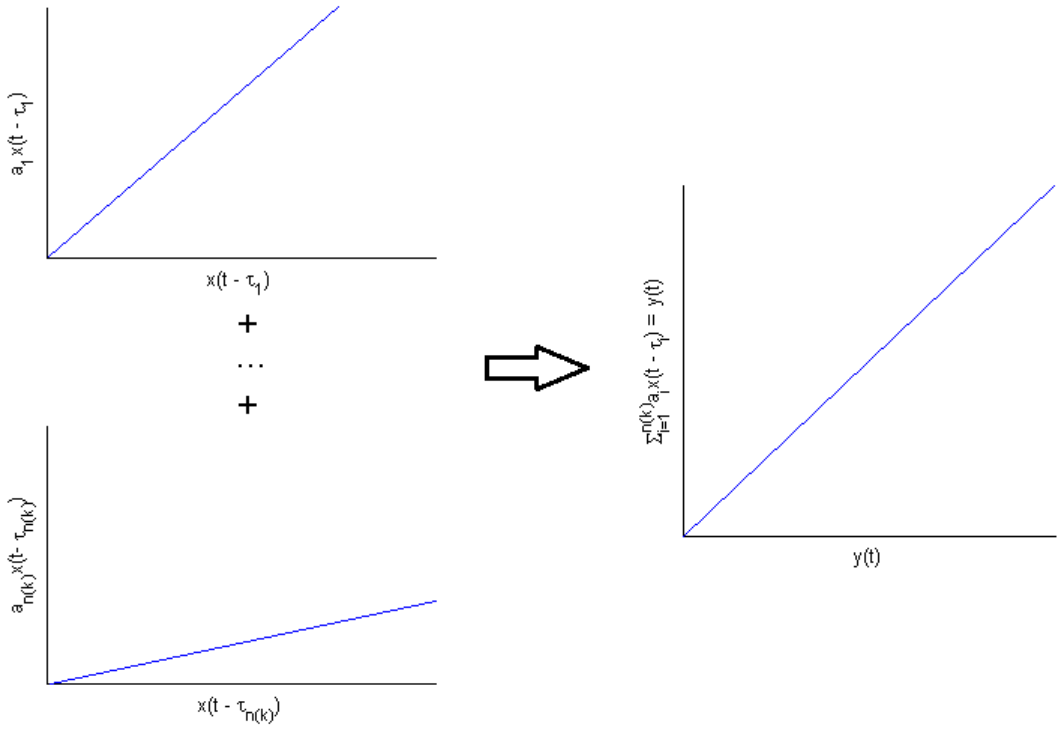

Figure 1.5: Convolution model. The slopes, a_i, associated with consecutive time lags are positively correlated. This is usually imposed by introducing a penalty for large variances between consecutive slopes a_i.

Again the output is a combination of linear functions, each of which can be defined by a single parameter, a_i. The factor a_i weights the influence that the input τ_i time units ago, has on the output at the current time, t.

In terms of the deconvolution problem it should be noted that there is one unknown (a_i) for each time lag, i.e. each predictor. If the discretization for τ coincides with the measurement times, there will be N_k equations and $N(k) = N_k$ unknowns. The unknowns associated with the small time lags (a_i for small i) will appear in more of the equations than those associated with large time lags, and therefore the a_i for small i can be determined with more confidence. For real data sets with associated noise, the system will often be close to singular. A simple way to fix that is to reduce the number of

discretization points, i.e. time lags considered. Moreover, from the physics of the problem, one can usually deduce that $f(t)$ should be continuous. Thus, there should be a positive correlation between consecutive values of a_i. This is can be enforced by adding a regularization term to the solution method, as was done e.g. by Schroeter (2004), and Nomura and Horne (2009).

1.5.3 Multiple input convolution

The convolution model with N_j inputs affecting a single output, in continuous form, is:

$$y(t) = \sum_{j=1}^{N_j} \int_0^t x_j(t-\tau) f_j(\tau) d\tau \tag{2.38}$$

The discrete analog is:

$$y(t_k) = \sum_{j=1}^{N_j} \sum_{i=1}^{n(k,j)} a_{ij} x_j(t_k - \tau_{ij}) \tag{2.39}$$

The coefficients, $a_{ij} = f_j(\tau_i)\Delta\tau_i$, are analogous to what was seen for single well deconvolution. In terms of deconvolving (2.39), note that if there are N_k time measurements and the discretization of τ coincides with t, the number of equations is N_k but the number of unknowns is $N_j N_k$. This means that the system is highly underdetermined. To make up for this, the system is usually solved with a smaller number of discretization points and added regularization terms for consecutive a_{ij} in terms of i. Essentially, as the number of inputs, N_j, increases, the number of discretization points, $N(k,j)$, must decrease, and the reconstruction of $f(t)$ will be coarser. A graphical representation of multiple input convolution is given in Figure 1.6.

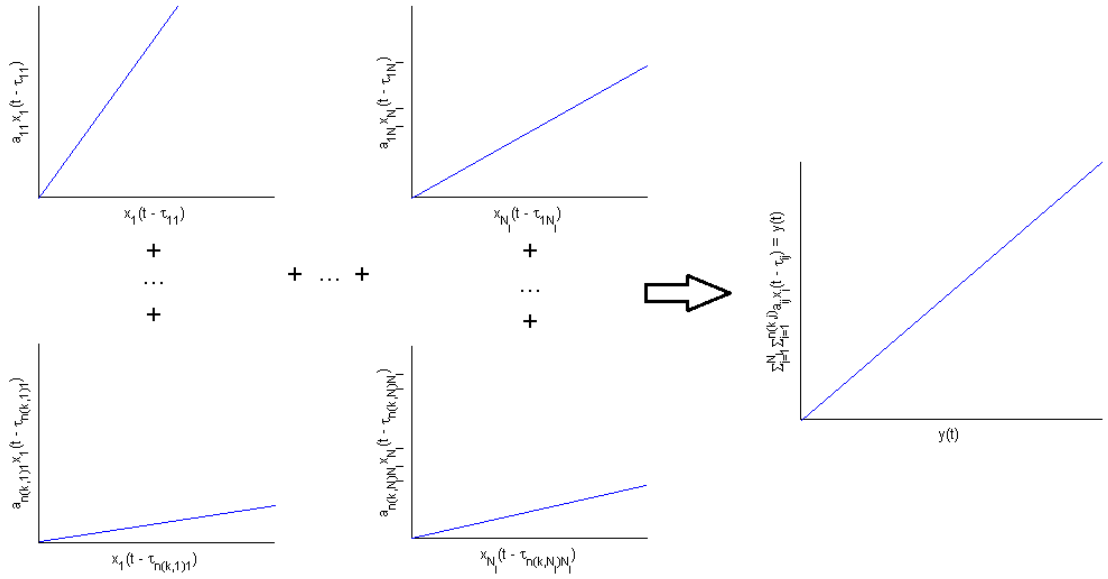

Figure 1.6: Multiple input convolution model. Generally the slopes, a_{ij}, associated with consecutive time lags are positively correlated, i.e. there is a positive correlation between the slopes going from top to bottom in the left part of the figure.

Multiple input deconvolution was applied for example by Lee et al. (2009) and in previous quarterly reports (summer 2009).

1.5.4 Alternating conditional expectation

The models that have been discussed so far can all be seen as linear regression models. That is, the output is a linear combination of multiple inputs, coming from different sources and with variable time lags. The alternating conditional expectation (ACE) model (Breiman and Friedman, 1985) is a more general model, in that it allows the functions of both the predictors and the responses to be nonlinear and nonparametric. The ACE model is as follows:

$$f\big(y(t)\big) = \sum_{j=1}^{N_j} g_j\left(x_j\big(t-\tau_j\big)\right) \tag{2.40}$$

The main restrictions on f and g_j are, that they must be smooth. This allows for great flexibility in fitting data, but the solutions will be highly susceptible to noise. This flexibility is perhaps more clear when viewing the discrete form:

$$f\left(y(t_k)\right) = \sum_{j=1}^{N_j} g_j\left(x_j\left(t_k - \tau_j\right)\right) \tag{2.41}$$

Note that $f\left(y(t_k)\right)$ and $g_j\left(x_j\left(t_k - \tau_j\right)\right)$ are simply scalars which are only restricted to have a positive correlation with nearby scalars in terms of k. The cost of this increased flexibility is that the predictive power of the ACE model will often be poor. Figure 1.7 illustrates the ACE model graphically.

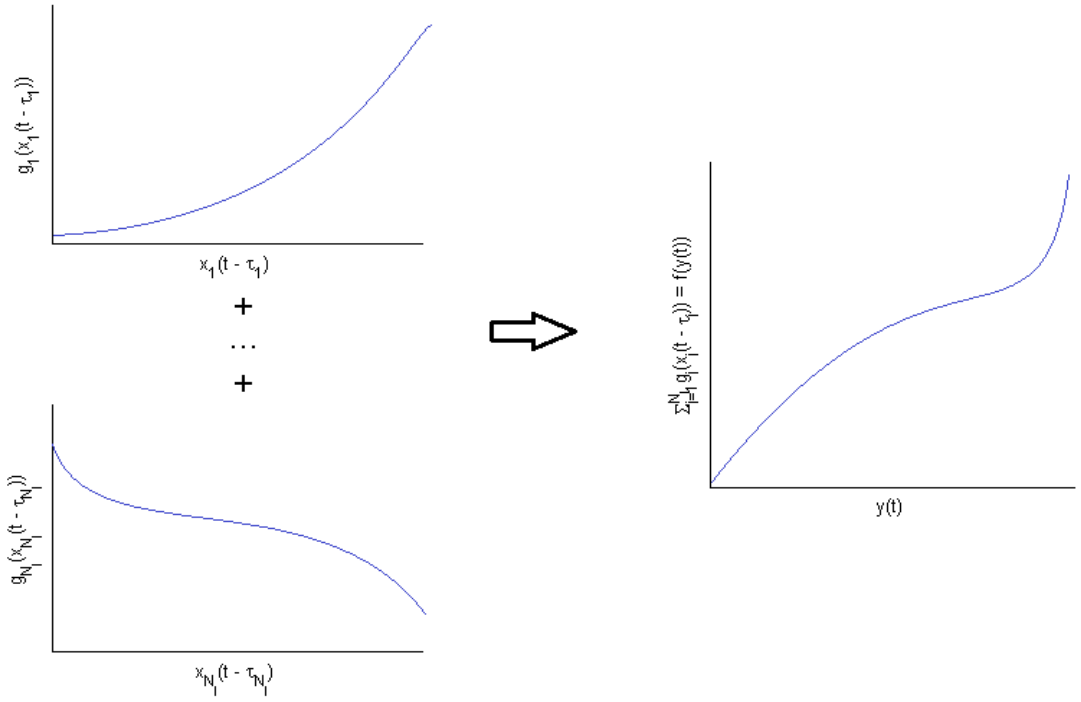

Figure 1.7: A graphical representation of the ACE model with inputs from multiple sources sampled with a possible time lag

The ACE model shown in (2.40) can be compared to the multiple input linear regression model (2.35). Note that simple straight lines which can be defined by a single parameter, have been replaced by a continuous sequences of N_k points. Thus the number of unknown variables for the model in (2.41) is $N_j N_k$. The ACE model was applied in the winter 2009 quarterly report and Horne and Schutz (2008). The ACE algorithm could also be used in an autoregressive manner, much like the M-ARX model. We experimented with this approach, but found that it had stability issues, and poor predictive power.

One of the drawbacks of using ACE is in the way described by Equation (2.40) is that this model assumes that the output is depend on each source with a unique time lag for

each source. However, the physics indicate that the response is a function of each source with multiple time lags. The ACE model could easily be used to take in data with multiple time lags as predictors, i.e.:

$$f\big(y(t)\big) = \sum_{j=1}^{N_j} \sum_{i=1}^{n} g_{ij}\left(x_j\big(t-\tau_{ij}\big)\right) \tag{2.42}$$

where n denotes the number of time lags taken into account. The graphical representation is shown in Figure 1.8.

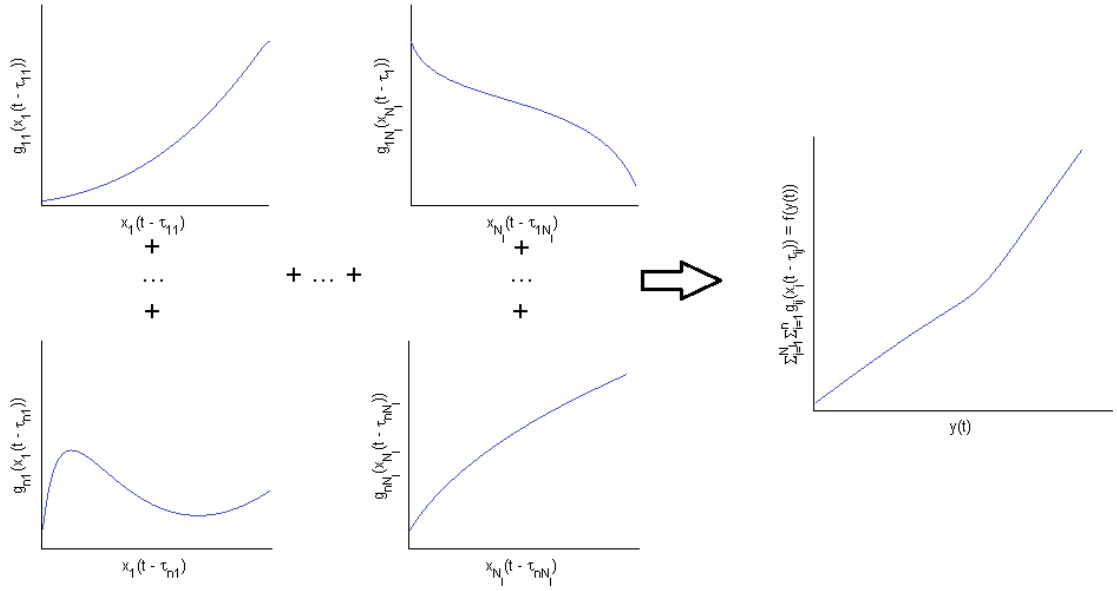

Figure 1.8: A graphical representation of the ACE model with inputs from multiple sources sampled with multiple time lag

Although this model would be exceptionally robust in fitting data, its predictive power would most likely be very poor. The number of equations in this case would be N_k and the number of unknowns $N_j N_k^2$. Additional constraints might be applicable to the model, e.g. by requiring there to be some sort of continuity between consecutive functions g_{ij} in terms of i. The details of how to impose such a continuity constraint is not clear at this point. It might also be possible to use an alternative predictor, e.g. cumulative flow rate, to make the predictions of ACE more unique and meaningful.

When using such a flexible regression method, the nature of the problem at hand should be carefully examined, since the nonuniqueness of the solution may lead to deceptively good data fits with poor representation of the physics of the problem. This may in some cases be avoided by choosing the predictors and responses carefully (e.g. based on physical intuition), and using a more restrictive regression model.

1.6 FUTURE WORK

A few fundamental results of the advection-dispersion equation with time-varying coefficients were introduced in this report. This raises questions about whether similar results can be found for slightly more complex, but physically more realistic cases. For example, can multidimensional versions, or the matrix diffusion model used by Jansen and Horne (1983) be rewritten in terms of cumulative injection? Moreover, will the convolution model hold for more general cases, thus allowing the estimation of nonparametric transfer functions in terms of cumulative injection using a deconvolution approach. And perhaps most importantly, can the appropriate cumulative injection be determined when there are multiple wells flowing simultaneously.

The estimation of interwell connectivity using a combination of rate data and tracer data should be tested using numerical modeling. Some work has already been done in this area, but numerical instabilities have caused progress to be slow. Once these problems have been solved we envision either continuing on, to work on optimization of reinjection scheduling, or moving the focus to interpretation of temperature signals. The reinjection scheduling problem could be tackled using a combination of the interwell conductivity parameters from the M-ARX model, and the interwell conductivity functions for tracer transfer, given in terms of cumulative flow rate.

The solutions for the time varying advection-dispersion could also be added into the discrete fracture simulator developed in previous quarterly reports.

1.7 CONCLUSIONS

In this quarterly report we have presented a solution to the one-dimensional advection-dispersion equation with time-varying coefficients. This solution has not been presented in the solute transport literature to our knowledge, although a similar conclusion in discrete and rather convoluted form was derived by Carlier (2008). We derived the solution for a single case of boundary and initial conditions, but the fundamental idea looks like it may be applicable to several other cases, even in higher dimensions. Moreover, we introduced a representation of the tracer kernel in terms of cumulative injection. This removes its explicit dependence on the flow rate, which allows for a more general interpretation. Some simplifying assumptions were made about the relationship between dispersivity and flow rate, and thus it remains to be seen how applicable this transformation is for more general cases.

The second part of this report gave a brief overview of models that have been used to describe rate-pressure, pressure-pressure and rate-rate interactions between wells. We attempted to give the most general form of the equations used in each case, along with the key tricks and assumptions used. The development of the rate-rate models was followed a bit more closely than the others. This was done mostly for the benefit of our understanding of how they work, and the fact that they seem particularly practical for large scale estimation and prediction.

The third section provided a relatively abstract overview of the regression models that have been used so far in relation to this research project. The section builds incrementally from relatively simple multiple input linear regression models to nonlinear nonparametric regression models with multiple inputs and multiple time lags (i.e. ACE). We also tried to analyze advantages and disadvantages of each method, and how more free parameters lead to better data fits but poorer predictive capabilities.

2. FRACTURE CHARACTERIZATION OF ENHANCED GEOTHERMAL SYSTEMS USING NANOPARTICLES

This project is being conducted by Research Assistants Mohammed Alaskar, Morgan Ames and Chong Liu, Senior Research Engineer Kewen Li and Professor Roland Horne. The objective of this study is to develop in-situ multifunction nanosensors for the characterization of Enhanced Geothermal Systems (EGS).

2.1 SUMMARY

Iron oxide (Fe_2O_3) nanorice coated with surfactant (PVP) injection was conducted to explore the mobility of rod-like nanoparticles through a slim tube packed glass beads. Glass beads were used to study the iron oxide transport within a porous medium in the absence of the rock materials. The constraint imposed by the surface charge of rod-like nanoparticles was investigated. The surfactant coating of the nanoparticles modified their surface charge. Both the particles and flow medium have negative charge. Coated iron oxide particles were not identified in the effluent collected from the slim tube.

Spherical silver nanoparticles were injected into Berea sandstone. The injection serves as preliminary testing of injecting metal alloys (tin-bismuth), which might be used as temperature sensors in geothermal reservoirs. The silver nanoparticles were identified in the effluent samples using SEM imaging. Their concentrations were determined by measuring their absorption using UV-visible spectrophotometry. The return curve showed that less than 25% of injected nanoparticles were recovered.

The sonochemical synthesis of tin-bismuth alloy nanoparticles with a eutectic composition was performed. The tin-bismuth alloy has a melting point at temperatures of geothermal interest, which may make them suitable as temperature-indicative nanotracers. The nanoparticles were characterized using dynamic light scattering (DLS) and scanning electron microscopy (SEM) imaging. A sample of these alloy nanoparticles was subjected to a heating experiment to begin investigating their melting properties. This sample was then also characterized using DLS and SEM imaging.

This report describes the results of the coated iron oxide nanoparticle injection into the packed slim tube, the spherical silver nanoparticles injection into Berea sandstone, and a bench heating experiment of tin-bismuth alloy nanoparticles. Characterizations of the iron oxide coated with PVP, silver nanoparticles, and tin-bismuth alloy nanoparticles are addressed. Standard measurements of porosity and permeability are also included.

2.2 INTRODUCTION

Last quarter (April-June 2010), iron oxide (hematite) nanorice injection experiments were carried out using Berea sandstone and a slim tube packed with glass beads. Influent and effluent samples were analyzed using DLS, UV-visible spectrophotometry and scanning electron microscopy (SEM). Iron oxide nanorice were not identified in effluent collected during the injection into Berea sandstone. DLS, UV-visible spectroscopy and scanning electron microscopy were used to examine the effluent samples, in which no nanoparticles

were detected. The iron oxide nanorice was, however, observed within the pores at the inlet side of the core. The iron oxide exhibited very low mobility during its injection through the slim tube packed with glass beads. The absorption of nanoparticles using UV-visible spectrophotometry could not be measured due to their low concentrations, and thus, the concentration of iron oxide nanoparticles in the effluent relative to the concentration in the influent could not be determined. To better understand the relationship between particle geometry and transport, the iron oxide was coated with SiO_2 and the surfactants TEA and PVP. Finally, the investigation of temperature-sensitive nanoparticles began with the synthesis of Sn-Bi alloy nanoparticles. The first attempt at the synthesis led to unsuccessful DLS measurements, either due to low ultrasonic power or an ineffective washing process.

During this quarter, the iron oxide coated with surfactant (PVP) was injected into a tube packed with glass beads. The influent and effluent samples were characterized using scanning electron microscopy. Also, a second flow experiment using spherical silver nanoparticles injected into Berea sandstone was conducted. The concentration of silver nanoparticles in the effluent samples was measured using UV-visible spectrophotometry by measuring the nanoparticles absorption and relating it to particle concentration using a calibration curve. The return curve of the silver nanoparticles production was determined. Standard measurements on the core sample were also performed. These measurements included the gas and liquid permeability, porosity and pore volume measurements. Finally, the Sn-Bi alloy nanoparticle synthesis was repeated, and the particles were characterized successfully using DLS and SEM imaging. A sample of these particles was subjected to a heating test to investigate their melting behavior. This heated sample was also characterized using DLS and SEM imaging. For the heated sample, the DLS results showed a wider particle size distribution which included larger particles. SEM images showed agreement with the DLS results as well as visual clues that melting had occurred. However, due to the wide distributions of sizes in both the original and heated samples, rigorous analysis of size change due to melting could not be achieved based on the SEM images.

2.3 BEREA SANDSTONE AND SLIM TUBE CHARACTERIZATION

This section describes the measurements of the porosity, permeability and pore volume of Berea sandstone and slim tube packed with glass beads used in the silver nanoparticle and coated iron oxide nanorice injection experiments, respectively.

2.3.1 Berea Core Characterization

The core sample tested was Berea sandstone of 3.8 cm in diameter and 4.1 cm in length. The gas and liquid permeabilities were determined. The Klinkenberg (gas slippage) effect was considered to evaluate the equivalent liquid permeability. Then, the liquid permeability for the same core sample was carried out. Porosity and permeability results are summarized in Table 2.1. Note that this is the same core sample used previously in the iron oxide injection reported last quarter (April-June 2010), except that the core sample was shortened. So the rock properties of porosity and permeability are the same. The pore volume, however, has changed from 9 ml to 8 ml.

Table 2.1: Berea porosity and permeability measurements summary

Property	Measurement method	Value
Porosity (%)	Saturation with deionized water	17.1
Permeability (md)	Nitrogen permeability at 1.43 atm.a	152
	Equivalent liquid permeability	72.2
	Liquid permeability	60.7

Figure 2.1 is a schematic of the apparatus used in the measurement of gas permeability. The gas flowed in this experiment was nitrogen (N_2). The inlet and outlet pressures were measured using standard pressure gauges. The flow rate at the outlet was measured using a stop-watch and graduated cylinder. Calibration curves were included in the January-March 2009 quarterly report.

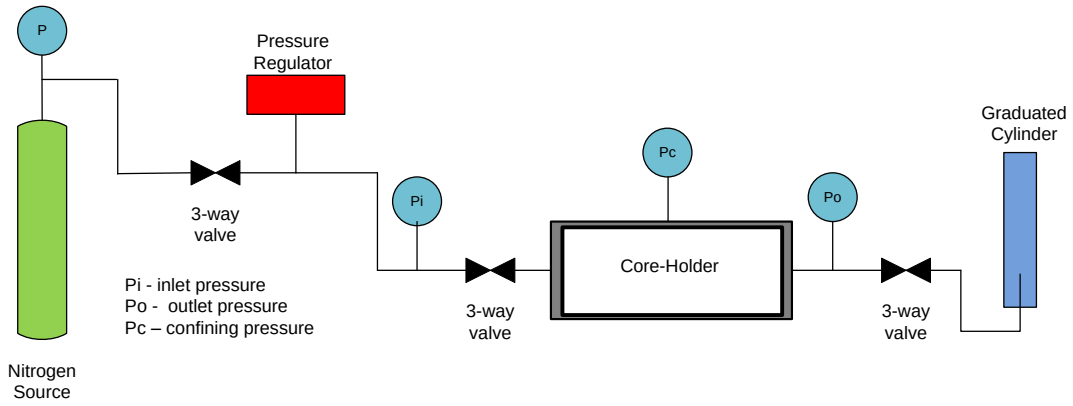

Figure 2.1: Schematic of the apparatus for measuring gas permeability.

The core was first dried in a furnace at 100°C under vacuum for 24 hours. After weighing the core sample, it was placed inside the core-holder under a confining pressure of 30 atm.g. The gas permeability measurement was then started by introducing nitrogen at different flow rates and inlet pressures. The average gas permeability was found to be around 152 millidarcy by applying Darcy's law for compressible fluids which is given by:

$$k_{gas} = \frac{2\mu p_{out} q_{out} L}{A(p_{in}^2 - p_{out}^2)} \tag{2.1}$$

where μ is the viscosity in centipoises, q_{tot} is outlet volumetric flow rate in cubic centimeter per second, A is the core cross-sectional area in square centimeter, L is the core length in centimeter and p_{in} and p_{out} are inlet and outlet absolute pressures in atmospheres, respectively.

The gas permeability as a function of the reciprocal of mean pressure is depicted in Figure 2.2. According to the Klinkenberg effect, extrapolating the straight line to infinite mean pressure (or zero reciprocal of mean pressure) intersects the permeability axis at a point designated as the equivalent liquid permeability (Amyx et al., 1960). In Figure 2.2, the average equivalent liquid permeability is approximately 72.2 millidarcy.

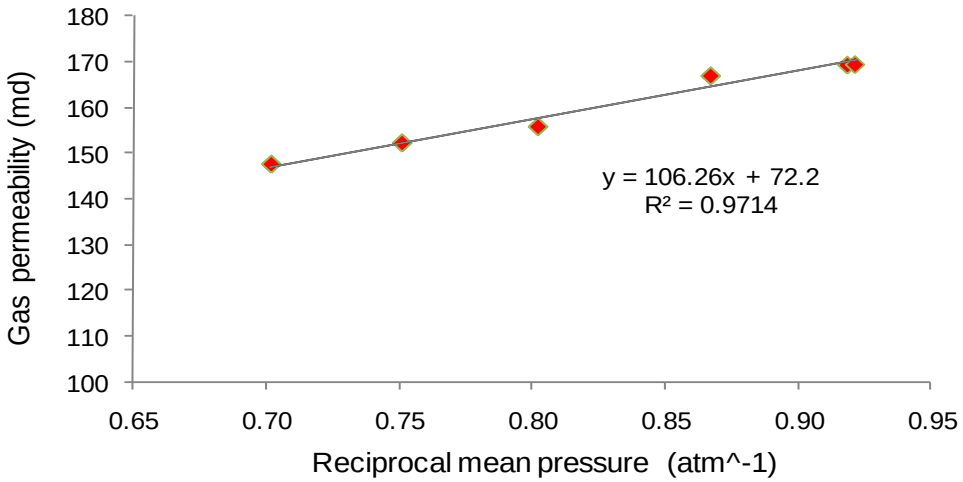

Figure 2.2: Berea core gas permeability versus the reciprocal of mean pressure.

The liquid permeability was measured on the same core sample directly. A schematic of the apparatus used in the measurement of liquid permeability is shown in Figure 2.3.

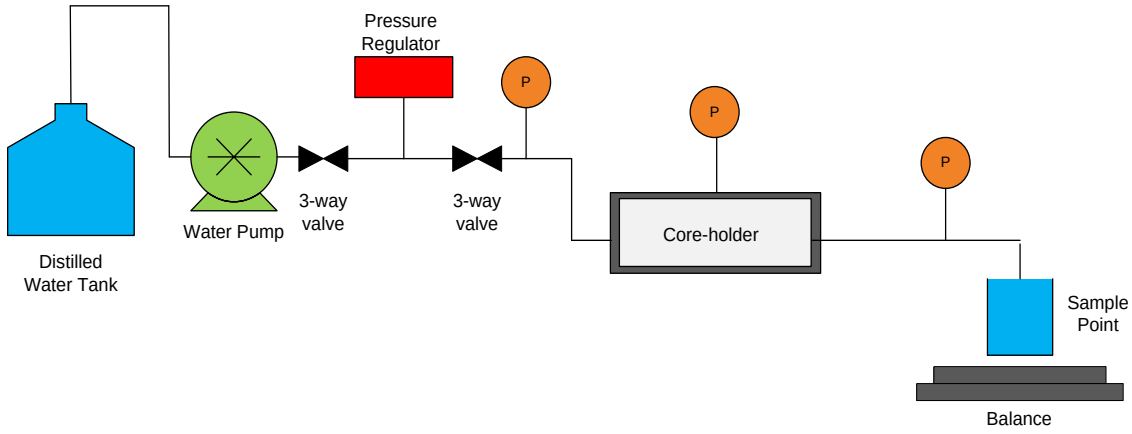

Figure 2.3: Schematic of apparatus for liquid permeability measurement.

The core sample was first saturated with water outside the core-holder. The core and related system were evacuated using a Welch Vacuum Pump for 4 hours at a vacuum pressure of about 20 millitorr to remove moisture. Pure water was introduced to completely submerge the sample. The core was then left submerged overnight and the remaining vacuum released to aid the process of saturation. After that the core was removed and wiped dry to remove excessive water on the surface. Finally, the core was weighed and hence its porosity was calculated. The core turned out to have a porosity of

around 17.1 % and a pore volume of 8 cubic centimeters. The porosity calculation is as follows:

$$\phi = \frac{V_p}{V_B} * 100 \tag{2.2}$$

$$V_p = W_s - W_d \tag{2.3}$$

$$V_B = \pi r^2 l \tag{2.4}$$

where ϕ is the porosity in percentage, V_p and V_B are pore and bulk volumes in cubic centimeter, respectively. W_s and W_d are the weight of core after and before saturation, in gram, respectively. r and l are the radius and length of the core in centimeter, respectively.

The average liquid permeability was found to be around 60.7 millidarcy. Darcy's law for horizontal flow was utilized to compute the permeability. Darcy's law for horizontal flow is given by:

$$k_{liq} = \frac{q\mu L}{A\Delta p} \tag{2.5}$$

where q is the volumetric flow rate in milliliter per second, μ is the viscosity in centipoise, L and A are the length and the cross-sectional area of the core in centimeter and square centimeter, respectively. Δp is the differential pressure across the core sample in atmospheres.

2.3.2 Polypropylene slim tube packed with glass beads

To investigate the mobility of iron oxide nanoparticles in the absence of rock materials (such as clays), the nanoparticles were injected into a slim tube packed with glass beads. A 30 cm long polypropylene slim tube was constructed. The tube was packed with glass beads (Glasperlen 1 mm in diameter from B. Braun Biotech International) and fitted with screens and valves at each end. This polypropylene slim tube is pictured in Figure 2.4. The porosity was measured by the saturation method. The porosity and pore volume of the glass bead packed slim tube were found to be approximately 46.8% and 2.39 ml, respectively. The permeability was estimated to be around 13 darcy.

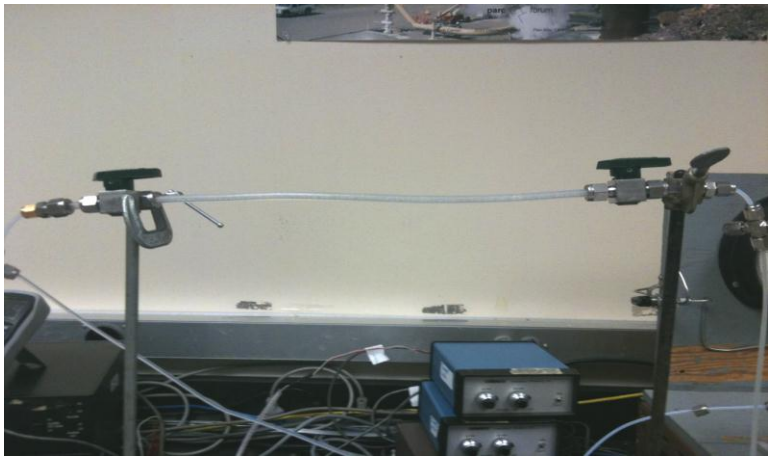

Figure 2.4: Polypropylene slim tube packed with glass beads

2.4 COATED IRON OXIDE CHARACTERIZATION AND INJECTION EXPERIMENT

In three different experiments, the iron oxide nanorice were coated with silica (SiO_2), the surfactants polyvinylpyrrolidone (PVP) and triethanolamine (TEA). The details of coating the iron oxide with the surfactants (PVP, TEA) or SiO_2 can be found in the last quarterly report (April-June 2010). The uncoated nanorice exhibited very low mobility during their injection through the glass bead packed slim tube (April-June 2010) which was attributed to their geometry and/or surface characteristics. To investigate further if the surface charge was limiting their flow, the nanorice were coated with the surfactants or silica to modify their surface charge.

2.4.1 Characterization of coated iron oxide

Coated iron oxide particles were characterized in terms of size, surface charge (zeta potential) and pH using SEM imaging, zeta potential analysis and pH meter, respectively. The original iron oxide nanoparticles were 500 nm in length and 100 nm in diameter. Surface charge and pH measurements are summarized in Table 2.2. The reported zeta potentials are the average of three sets of measurement with standard deviation less than 2.

Table 2.2: Zeta potential and pH level for original and coated iron oxide nanoparticles.

Sample	Average zeta potential (mV)	pH
Original Iron oxide	+59.3	3.3
Iron oxide-SiO_2	-32.4	5.56
Iron oxide-PVP	-9.5	4.82
Iron oxide-TEA	+18.9	4.5

Note that there were three identical iron oxide samples each coated with different material. It was evident from the surface charge measurements that the coating materials have

altered the surface charge of the original iron oxide nanorice. The original (uncoated) iron oxide nanorice carries a high positive charge of 59.3 mV with low pH of 3.3 compared to the samples coated with silica (negative 32.4 mV and 5.56 pH) and PVP surfactant (negative 9.5 mV and 4.82 pH). The iron oxide coated with TEA surfactant resulted in moderately positive charge of about 18.9 mV. The zeta potential distribution of original and coated iron oxide nanoparticles can be depicted in Figure 2.5.

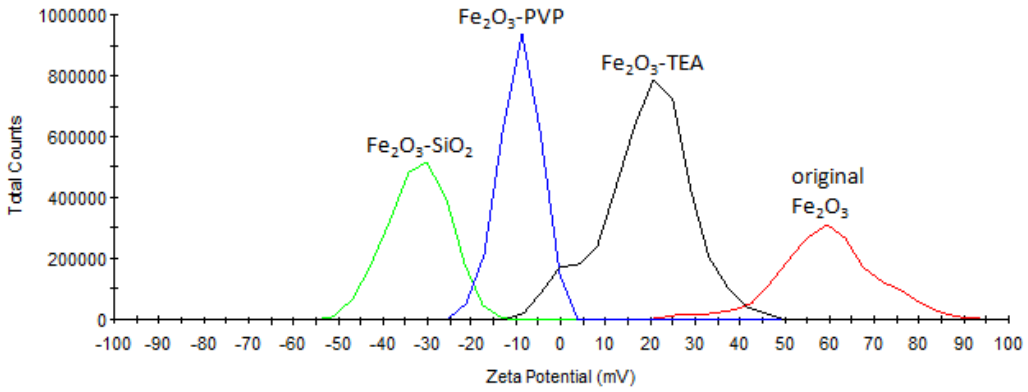

Figure 2.5: Zeta potential distribution of coated and uncoated iron oxide nanoparticles.

The glass beads used as the porous medium carry a negative charge. So it is of interest to inject particles that carry the same type of charge (i.e. negative charge), as similar charges repel and should prevent particle attachment to the glass beads. Based on this, the iron oxide nanoparticles coated with TEA surfactant were not selected for injection.

From the surface charge point of view, the iron oxide nanoparticles coated with SiO_2 were a very attractive candidate. They carry the highest negative surface charge among the three samples. Figure 2.6 shows the zeta potential distribution of silicon dioxide, iron oxides and silicon coated iron oxides. The peak of the distribution of the coated iron oxide nanorice is positioned between the peaks of the silicon dioxide and iron oxide.

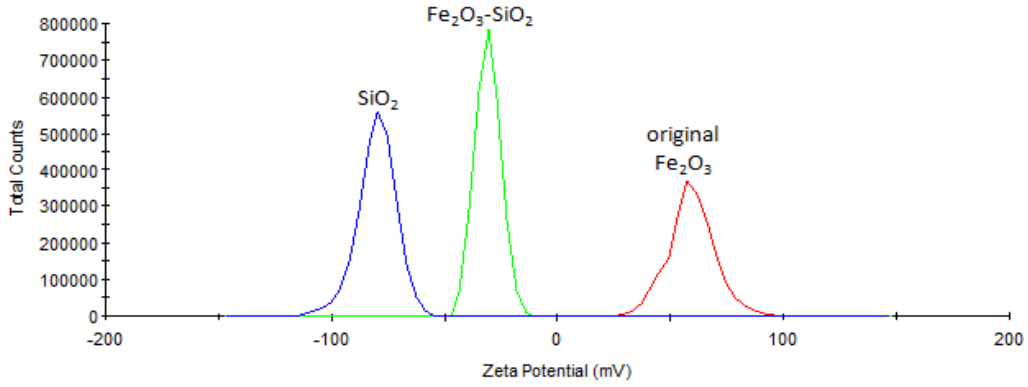

Figure 2.6: Zeta potential distribution of silicon only, iron oxide only and iron oxide nanoparticles coated with silica.

SEM imaging (Figure 2.7) showed that the iron oxide nanorice have a uniform SiO_2 coating of about 50 nm. As a result, the size of the iron oxide nanorices has changed from 500 nm and 100 nm to 600 nm and 200 nm in length and diameter, respectively. It was also observed that the nanorice did not retain their original spindle-like shape with sharp edges (Figure 2.7 B).

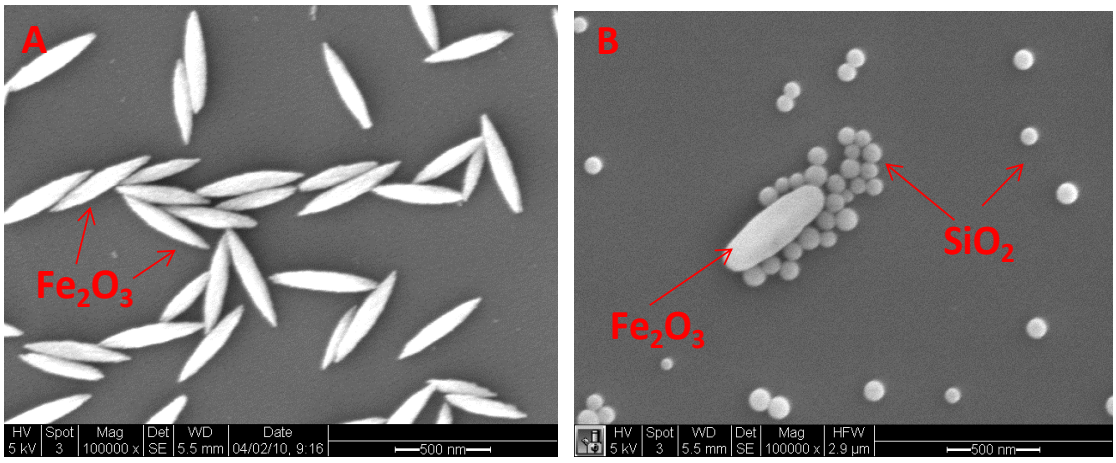

Figure 2.7: Iron oxide nanoparticles (A) before SiO_2 coating, (B) after coating with SiO_2. Coated sample did not retain its spindle-like shape as a result of the 50 nm SiO_2 coat.

Further evaluation of the nanorice coated with silica showed that the SiO_2 nanoparticles (about 100 nm in diameter) were dominating the sample. There were more SiO_2 nanoparticles than Fe_2O_3. The existence of excess SiO_2 nanoparticles resulted from the coating process. SEM image in Figure 2.8 is an example. Attempts to separate the silicon dioxide nanoparticles have not been successful and thus this nanofluid sample was not injected into the glass beads packed tube.

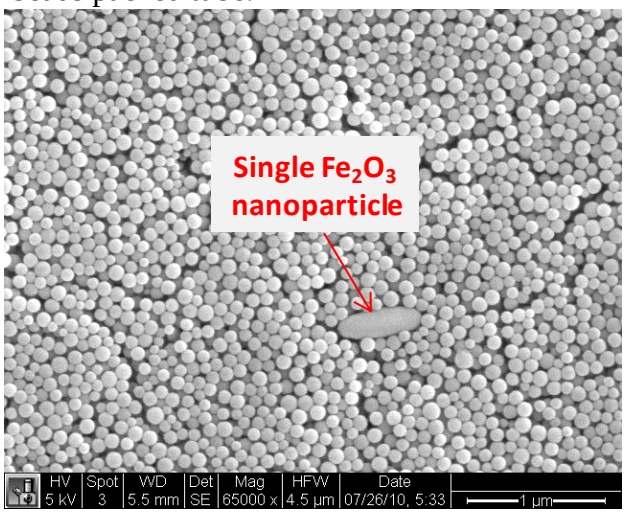

Figure 2.8: SEM image showing single iron oxide nanorice among the dominating silicon dioxide nanoparticles.

It was concluded that the iron oxide nanoparticles coated with SiO_2 and surfactant TEA were inappropriate for injection. However, iron oxide coated with surfactant PVP retained suitable characteristics in that it carried negative surface charge of 9.5 mV (Table 2.2). To

coat the iron oxide with PVP, a 0.1 M solution of PVP in ethanol was prepared. Iron oxide nanofluid was then added, sonicated for 1 hour, and soaked overnight. The coated particles were cleaned by centrifugation three times at 6.5 krpm to remove excess surfactant.

2.4.2 Iron oxide (Fe_2O_3) coated with surfactant (PVP) nanoparticle injection into glass beads packed slim tube

The iron oxide nanorice coated with PVP surfactant was injected into the slim tube packed with glass beads. A schematic of the apparatus used is depicted in Figure 2.9.

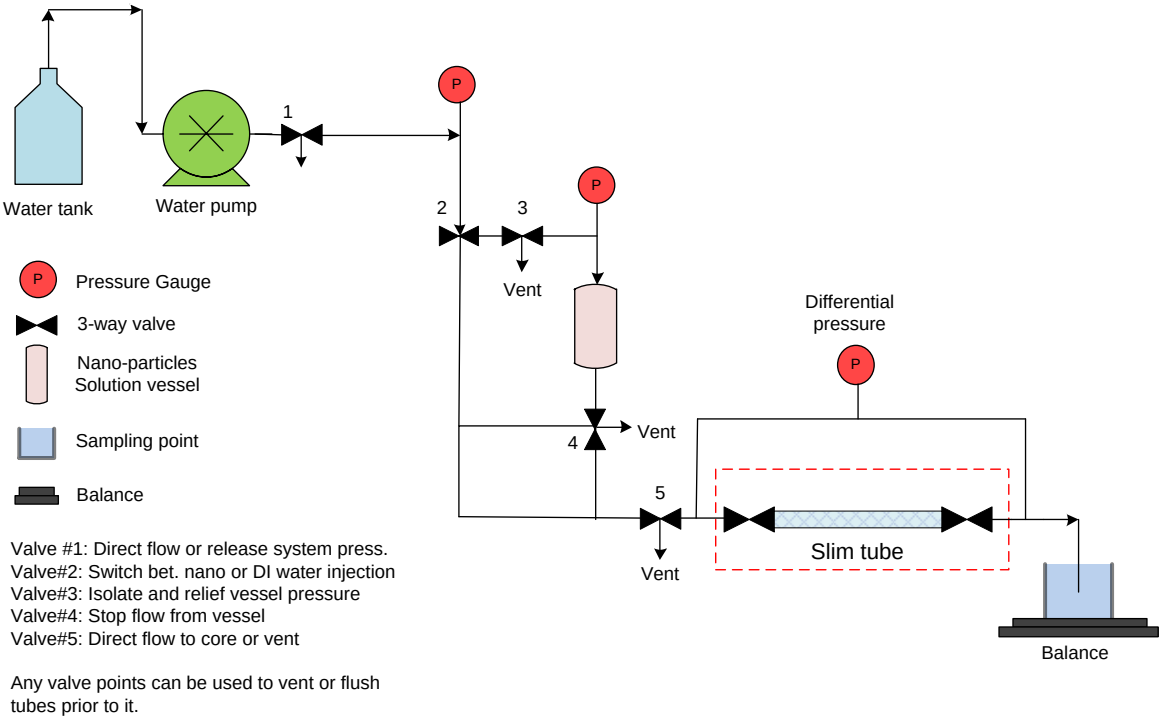

Figure 2.9: Experimental apparatus for nanofluid injection into glass beads packed tube.

The slim tube was initially preflushed with several pore volumes using pure water. Then, one pore volume of the iron oxide nanofluid was injected at differential pressure of about 0.14 atm. Following the nanofluid injection, 10 pore volumes of pure water was post injected at rate of 0.5 ml/min and eight effluent samples were collected. The permeability was not altered during or after the injection of the iron oxide.

2.5 SPHERICAL SILVER NANOPARTICLES CHARACTERIZATION AND INJECTION EXPERIMENT

The objective of this experiment was to investigate the transport and recovery of spherical silver nanoparticles through the pores of Berea sandstone. Initial testing with silver nanomaterial was conducted earlier with the injection of silver nanowires into Berea sandstone. The goal was to investigate the transport of a wire-like nanoparticle and experimentally verify if nanoparticles shape would initiate any complication to the particles flow. The silver nanowires were not detected in the effluent and were found

trapped at the inlet face within the pore spaces of the core rock. The details of the silver nanowires injections can be found in an earlier quarterly report (July-September 2009). The spherical silver nanoparticles injection serves as a preliminary to the testing of injecting spherical metal alloy (Tin-Bismuth) which might be used as temperature sensors in geothermal reservoirs.

2.5.1 Characterization of silver nanoparticles

Silver nanoparticles were characterized in terms of size, surface charge (zeta potential), light absorption and pH levels using SEM imaging, zeta potential analysis, UV-visible spectrophotometry and pH meter, respectively. The particle size was around 40 nm ±10 (Figure 2.10). The silver nanoparticles synthesis is a protocol adapted from Kim et al. (2006).

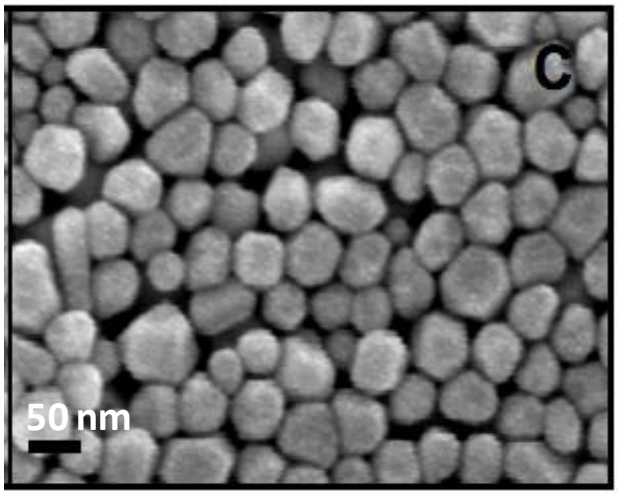

Figure 2.10 : SEM image of the silver nanoparticles.(Levard, personal communication)

The silver nanofluid sample volume was 20 ml with concentration of 1 g/l. the sample was sonicated for about 10 minutes using a Branson 2510 Sonicator prior to dilution. Then the nanofluid was diluted one part of silver nanofluid into two parts of pure water. The final concentration used in the injection experiment was 0.5 g/l.

The average zeta potential of the diluted silver nanoparticles sample was measured and found to be approximately negative 17 mV with standard deviation less than 2. The pH level was around 7.9. The zeta potential distribution of the silver nanoparticles is illustrated in Figure 2.11.

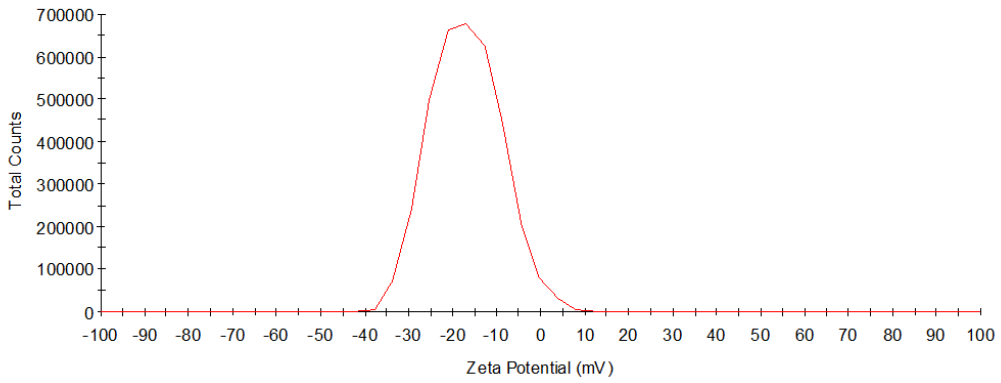

Figure 2.11: Zeta potential distribution of the silver nanoparticles.

UV-visible spectrophotometry was used to measure the absorption of the silver nanoparticles in effluent samples and hence their concentrations. This is an essential step as it enables us to construct the tracer return curve of concentrations verses volume injected. UV-visible spectrophotometry involves the spectroscopy of photons in the UV-visible region, which means that it deals with light in the visible, near-ultraviolet and near-infrared ranges. The spectrophotometer is the instrument used to measure the light intensity as a function of wavelength of light. Beer's Law is used to quantify the concentrations of absorbing species in solution (Wittung et al., 1994). The law states that the absorbance of a solution is directly proportional to the path length through the sample and the concentration of absorbing species in solution. Beer's Law is given by:

$$A = -\log_{10}(I / I_o) = \varepsilon c L \tag{2.6}$$

where A is the measured absorbance, I is the intensity of light passing through the sample, I_o is the intensity of light before it passes through the sample, L is path length through the sample, c is the concentration of absorbing species and ε is the molar absorptivity constant which is specific for each species and wavelength at particular temperature and pressure and has units of $AU / M * cm$.

Therefore, measuring the absorbance of the substance in solution and knowing the path length of the sample along with the absorptivity constant, the concentration of that substance can be calculated. Due to the difficulty in obtaining the absorptivity constant, it is common to determine the concentrations by constructing a calibration curve. This avoids having to rely on a value of the absorptivity or the reliability of Beer's Law. The calibration curve is accomplished by making few dilutions, each with accurately known concentration. It is important to ensure that those concentrations bracket the unknown concentrations under investigation. For each dilution, the absorbance is measured and plotted against the sample concentration. This is the calibration curve.

The original silver nanofluid was diluted one part of nanofluid to 100, 150, 200, 250, 300, 400 and 500 parts of pure water. Then, the absorbance spectra were measured at room

temperature using a Shimadzu UV-1700 double beam spectrophotometer with a 12 mm square polystyrene cuvette. All samples had been sonicated prior to analysis to disperse the particles. The optical (absorbance) signatures of the diluted silver nanofluid samples are shown in Figure 2.12.

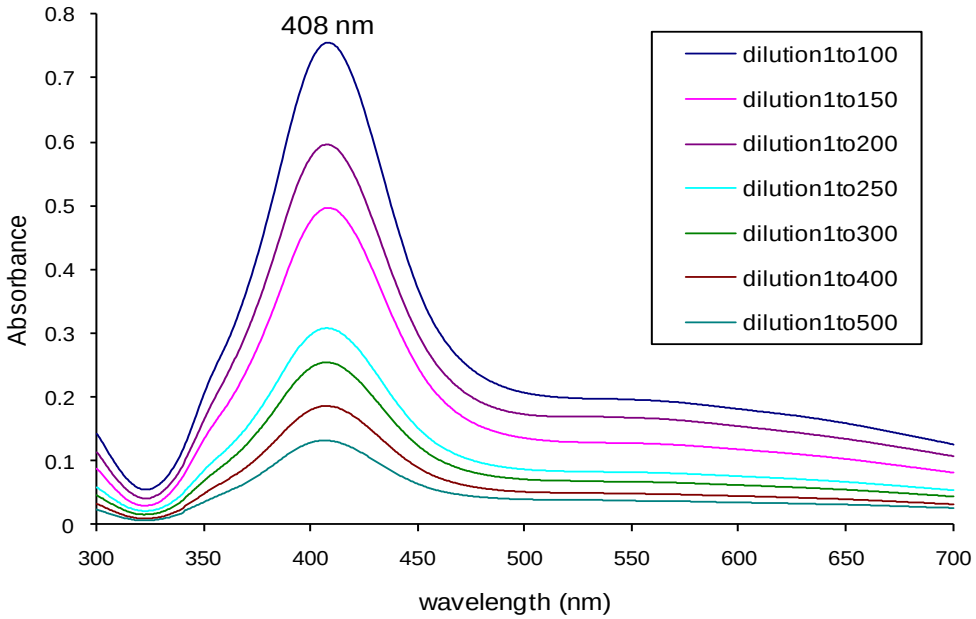

Figure 2.12: Absorbance of diluted silver nanofluids of known concentrations.

The absorbance readings were all taken at a wavelength of 408 nm, which is the wavelength at which the strongest (maximum) absorption occurs. The diluted sample concentrations and corresponding absorbance were used to construct the calibration curve (Figure 2.13). The calibration curve was used to determine the concentration of effluent samples using their absorbance.

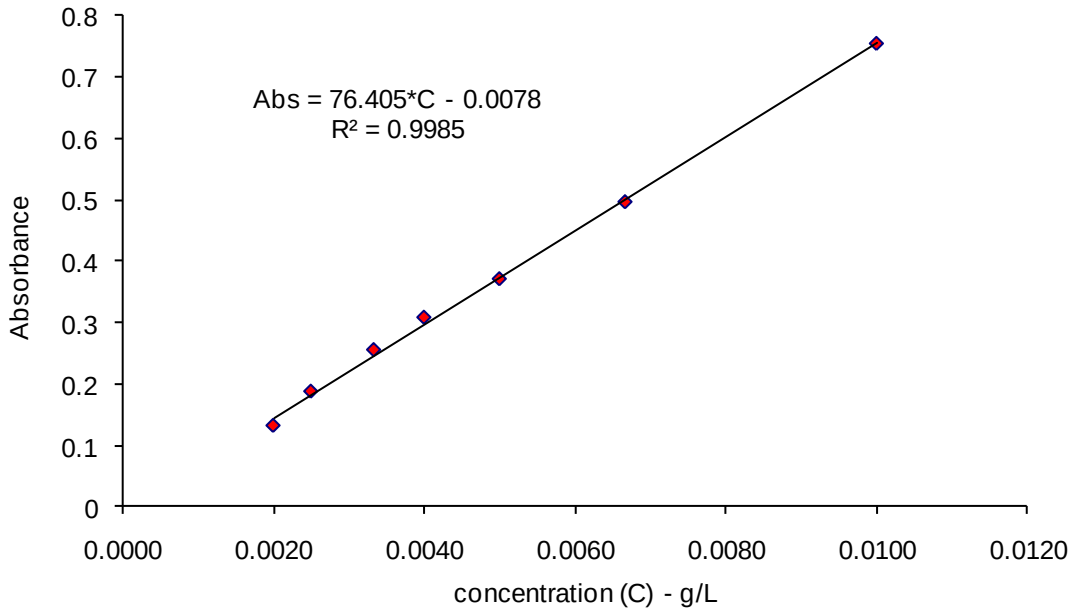

Figure 2.13: Calibration curve of silver nanofluid prepared for injection into Berea sandstone.

2.5.2 Silver nanoparticle injection into Berea sandstone

Silver nanoparticles injection was conducted to investigate their flow through the pores of Berea sandstone. A schematic of the apparatus is shown in Figure 2.14. Nanofluid solution was contained in a pressure vessel downstream of the water pump. The silver nanoparticles were injected with the aid of nitrogen gas. The configuration also allows for injection of particle-free water, without interrupting the flow. The silver nanoparticles were of an average size of 40 nm in diameter.

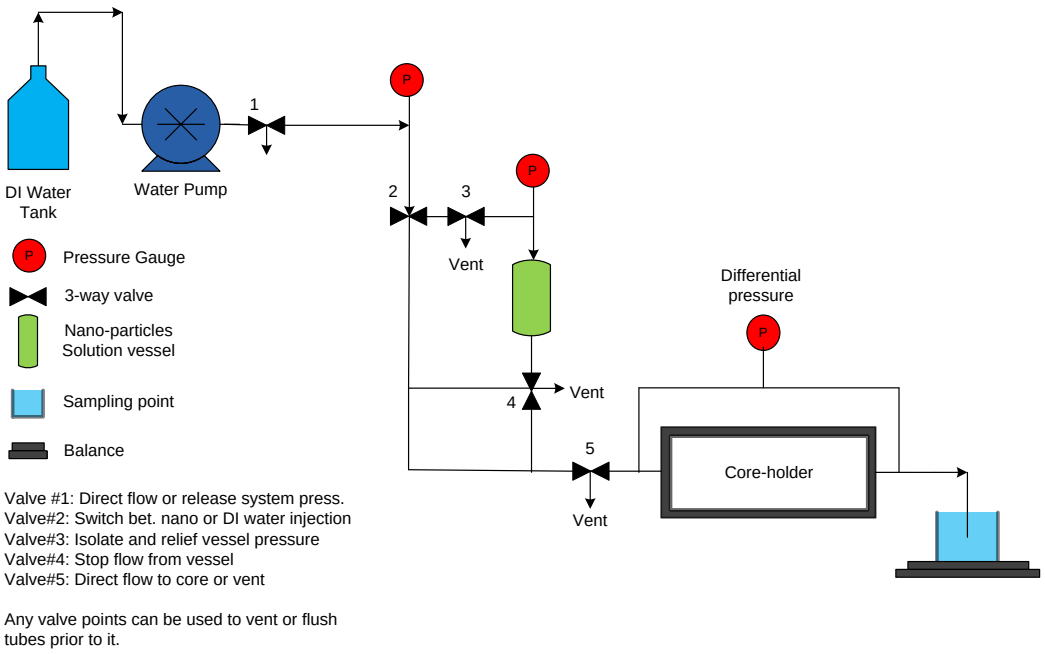

Figure 2.14: schematic of the silver nanofluid injection apparatus.

Prior to the injection of the nanofluid, the core was preflushed with pure water to displace as much rock fines and debris as possible. The nanofluid injection sequence was similar to the process suggested by Kanj et al. (2009). The sequence involved the injection of a certain volume of nanofluid followed by a continuous injection of pure water. In particular, 25% (2 ml of nanofluid) of the pore volume was injected. The silver nanofluid was diluted one part silver to ten parts of pure water.

Subsequent to the injection of the nanofluid, a continuous flow of pure water (post injection) was introduced. Specifically, four pore volumes of pure water were injected while the effluent samples were collected. The total time of the experiment was approximately 30 minutes. The injection was at the rate of 1 milliliter per minute at a differential pressure of about 6.25 psig. A total of 12 effluent samples were collected at the rate of 2.5 milliliter per sample. All these samples were analyzed using UV-visible spectrophotometry. Samples from the first and third pore volumes were analyzed using SEM.

2.6 SYNTHESIS, CHARACTERIZATION, AND HEATING TEST OF TIN-BISMUTH ALLOY NANOPARTICLES

In our second attempt to investigate temperature-sensitive nanoparticles, the sonochemical synthesis of tin-bismuth alloy nanoparticles of eutectic composition was repeated at a higher ultrasonic power. These particles were characterized using DLS and SEM imaging. A bench heating experiment was also performed to study the thermal sensitivity of these nanoparticles. The sample subjected to heating was then characterized with DLS and SEM imaging.

2.6.1 Synthesis of tin-bismuth alloy nanoparticles

To perform the synthesis, Sn and Bi were melted together at the eutectic composition (~60 wt % Bi and ~40 wt % Sn). After the alloy was cooled to room temperature, 100 mg was sonicated in 10 ml of mineral oil, a slight variation of the sonochemical method suggested by Chen (2005). The VC-505 ultrasonic processor manufactured by Sonics & Materials, Inc. with a 0.75 in. diameter high gain solid probe was used. The sonicator was operated at 200 W (~95% amplitude) with a pulse setting of 20 s on, 10 s off. The mixture was cooled to room temperature. The alloy particles were washed and centrifuged several times with a 1:1 mixture of hexane and acetone, rinsed in a solution of 0.1 M PVP in ethanol, and finally suspended in ethanol. The centrifuge setting was 6000 rpm for 15 minutes each time.

2.6.2 Characterization of tin-bismuth alloy nanoparticles

The tin-bismuth alloy nanoparticles were characterized in terms of size and shape using DLS and SEM imaging.

It was determined from three consecutive DLS measurements that there was a wide distribution of the particle hydrodynamic diameter, as shown in Figure 2.15.

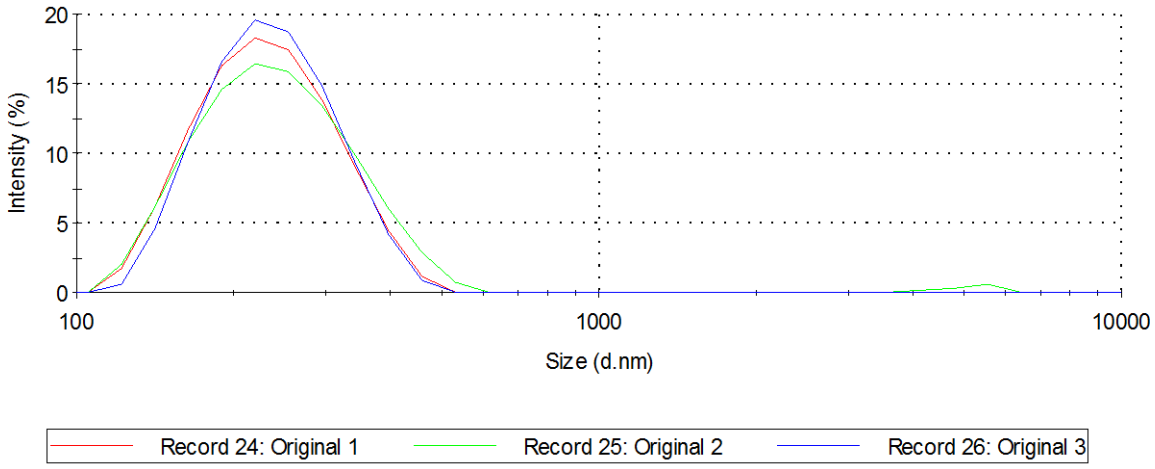

Figure 2.15: Logarithmic particle size distribution based on hydrodynamic diameter for original Sn-Bi nanoparticle sample.

It is believed that the improved washing technique (using a mixture of hexane and acetone instead of ethanol) allowed the particles to be well dispersed in ethanol, which in turn allowed successful DLS measurements. The three measurements are in relatively close agreement, with a standard deviation of about ±2 nm and an average modal value of 235 nm. The hydrodynamic diameter ranged from ~100 nm to ~600 nm, with Run 2 showing a small peak at ~5500 nm. This indicates that there may have been large particles in the sample, either due to aggregation or from the original synthesis.

The SEM images of the sample show good agreement with the DLS measurements, as shown in Figures 2.16 and 2.17.

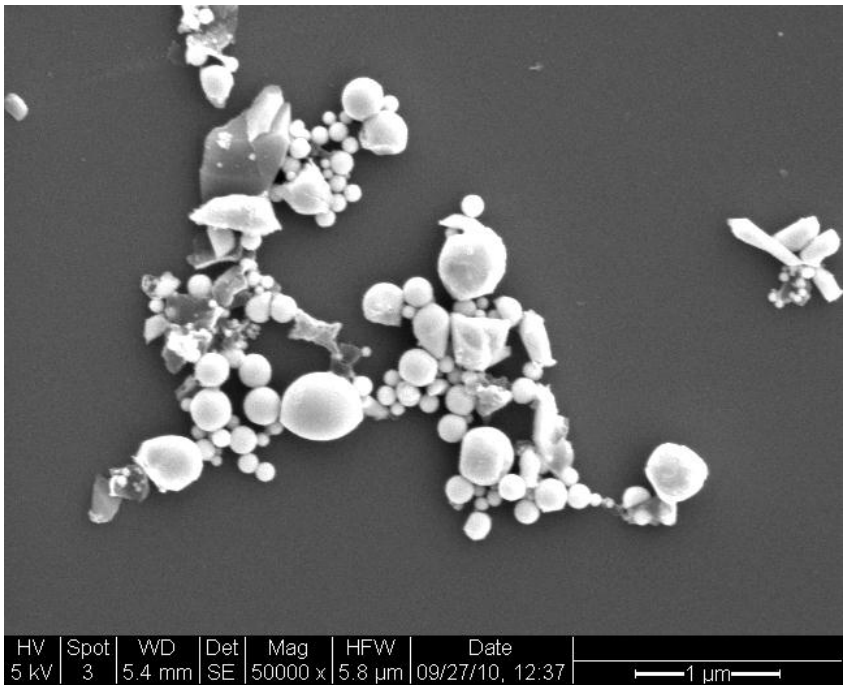

Figure 2.16: SEM image showing the wide range of Sn-Bi nanoparticle sizes.

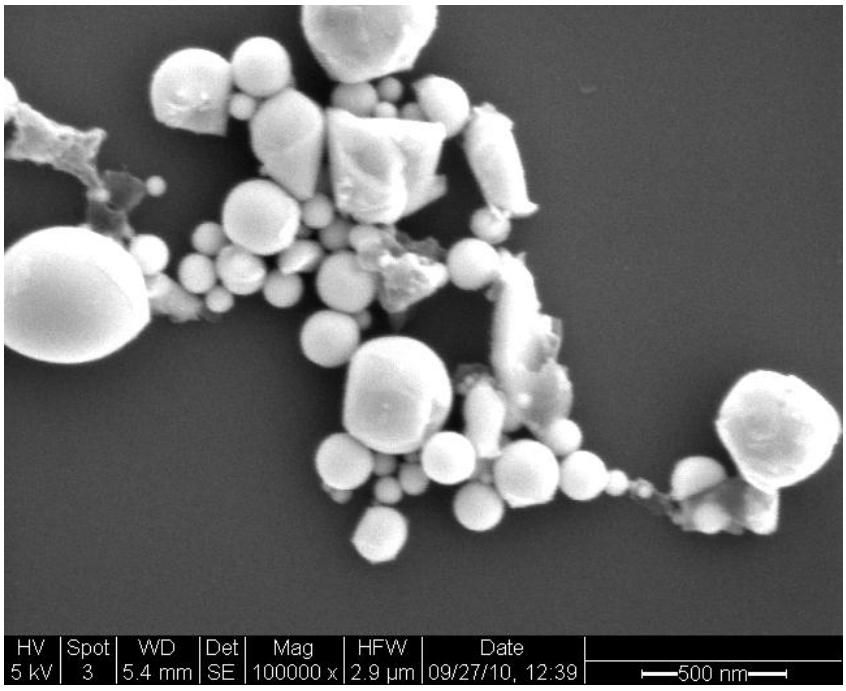

Figure 2.17: SEM image of Sn-Bi nanoparticles showing the same area of the sample at higher magnification.

It is apparent from Figures 2.16 and 2.17 that the "bare" Sn-Bi nanoparticles range from <100 nm to >500 nm. Furthermore, although many of the nanoparticles seem to be

spherical as expected, the presence of nonspherical crystalline structures indicates that the sonochemical synthesis did not reach completion. Aggregation on the substrate is observed in both figures, but it is unclear whether this aggregation occurs in solution or upon drying on the substrate. The DLS results suggest that the latter may be the case.

2.6.3 Heating experiment

To begin investigating particle melting and cooling behavior within the temperature range of interest, a sample of the nanofluid (Sn-Bi in mineral oil) from the synthesis described in Section 2.6.1 was subjected to a preliminary heating experiment. Although we are ultimately interested in the melting behavior of the Sn-Bi nanoparticles in water, the heating experiments were performed in oil due to the complications associated with the boiling of water at experimental conditions. As shown in the phase diagram Figure 2.18, at the eutectic composition, the Sn-Bi alloy melts at 139°C. In fact, the nanoparticles probably melt at a slightly lower temperature than this due to melting point depression.

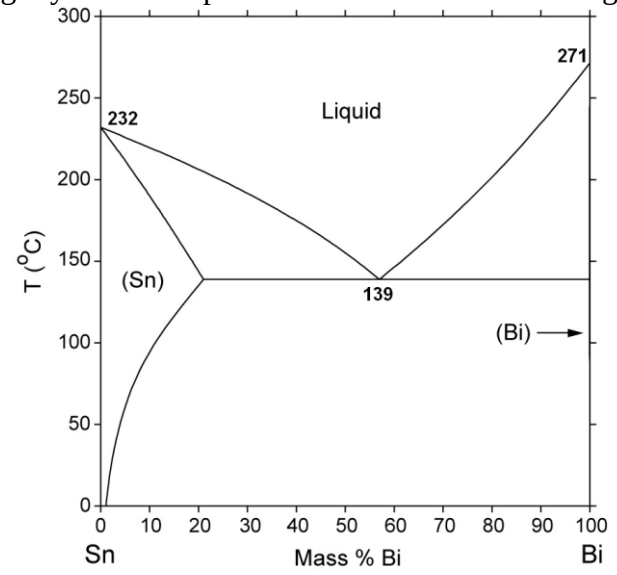

Figure 2.18: Phase diagram of Sn-Bi *(NIST)*.

The experiment used to heat the sample included a heating mantle connected to a temperature controller with a feedback thermometer as shown in Figure 2.19.

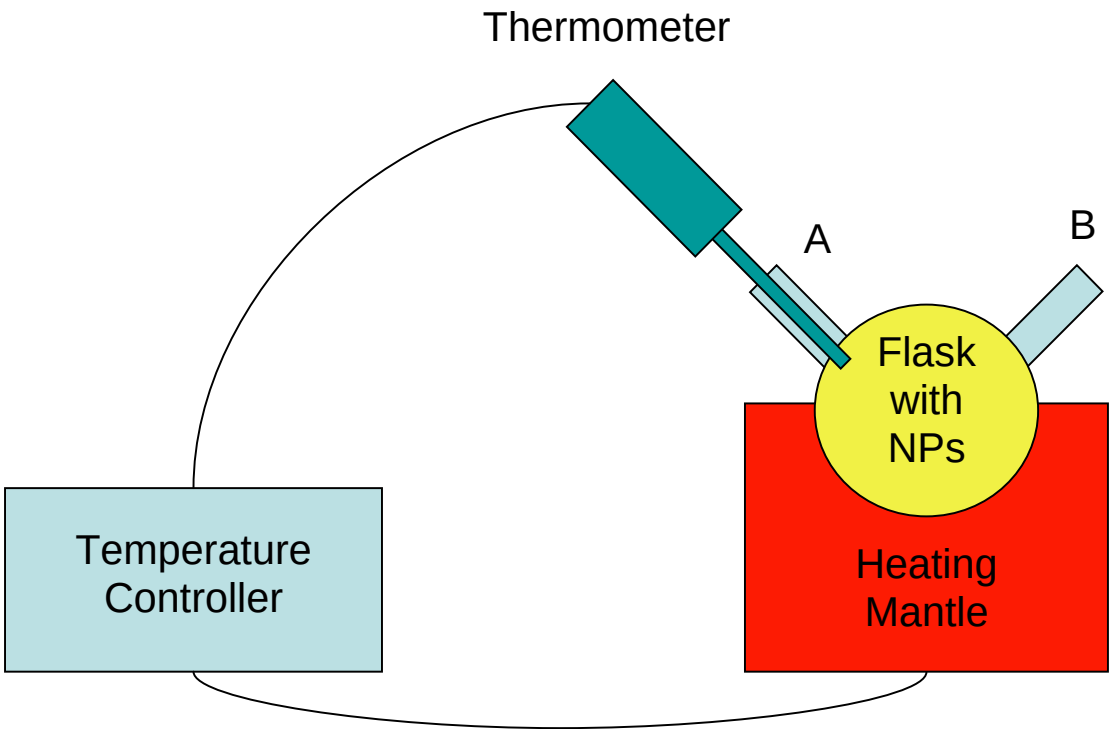

Figure 2.19: Experimental apparatus for Sn-Bi heating experiment

The flask containing the Sn-Bi nanoparticles in oil was placed in the heating mantle, which was connected to the temperature controller. The temperature controller was also connected to a thermometer, the feedback from which affected whether the mantle was heated, cooled, or maintained and the rate at which this was done. The thermometer was positioned in port A.

The sample was heated in steps to the expected melting point of 139°C. The sample was monitored for a color change near the expected melting point, and when none occurred, the sample was heated in steps to 210°C. No color change ever occurred, but the heating was stopped to prevent the mineral oil from burning. Also, it was assumed that melting had probably occurred regardless of the absence of color change. Finally, when the apparatus was at room temperature, the sample was removed from the flask. Then the sample was washed and centrifuged several times with a 1:1 mixture of hexane and acetone, rinsed in a solution of 0.1 M PVP in ethanol, and finally suspended in ethanol. The centrifuge setting was 6000 rpm for 15 minutes each time. This sample was then characterized using DLS and SEM imaging.

2.7 RESULTS

During this quarter, three experiments were conducted. Two main flow experiments included the injection of iron oxide coated with surfactant (PVP) into the tube packed with glass beads and the injection of spherical silver nanoparticles into a Berea sandstone. The third experiment involved heating the Sn-Bi alloy nanoparticles.

In order to determine whether the transport of iron oxide nanorice was limited by their surface characteristics, iron oxide was coated with SiO_2 and the surfactants TEA and PVP to modify its surface properties. Among all, iron oxide coated with PVP has been selected for injection as outlined in Section 2.4.1. Effluent samples at the first and second pore volume injected as well as the actual glass beads from the inlet and outlet were examined under SEM. The coated iron oxide was neither detected at the effluent samples nor within the glass beads. Note that testing the hypothesis made regarding the entrapment of iron oxide nanorice due to their geometrical size (length) was tested previously and details can be found in last quarterly report (April-June 2010).

The second experiment involved the injection of spherical silver nanoparticles into Berea sandstone. The silver nanoparticles were transported through the pore space of the rock and were detected in the effluents. SEM imaging has confirmed the transport of the nanoparticles as shown in Figure 2.20.

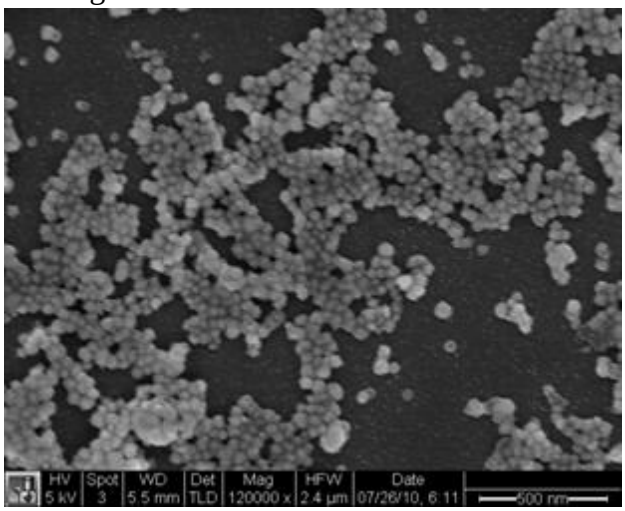

Figure 2.20: SEM image of effluent sample taken from the third post injected pore volume.

The recovery of the silver nanoparticles can be observed visually, as shown in Figure 2.21. Cloudy samples are highly concentrated with silver nanoparticles compared to transparent samples. It could also be seen visually that the nanoparticles were recovered following the post injection of about 60% of the first pore volume of pure water and produced continuously until the bulk of these particles were displaced through the second pore volume.

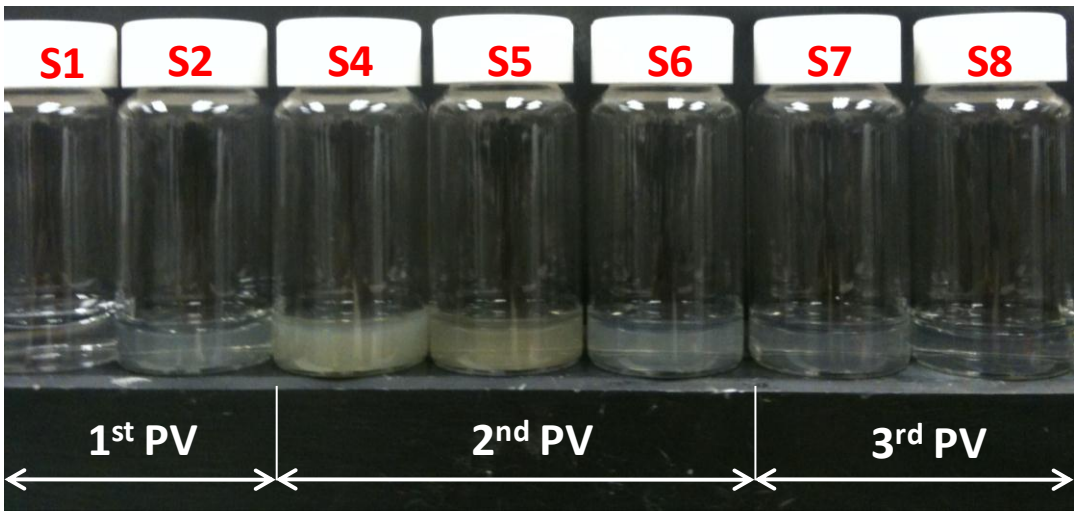

Figure 2.21: Visual characterization of effluent samples for their silver nanoparticles content based on color.

The concentration of the effluent samples was determined by measuring their absorbance using the UV-visible spectrophotometry. The absorption spectra for all effluent samples are depicted in Figure 2.22.

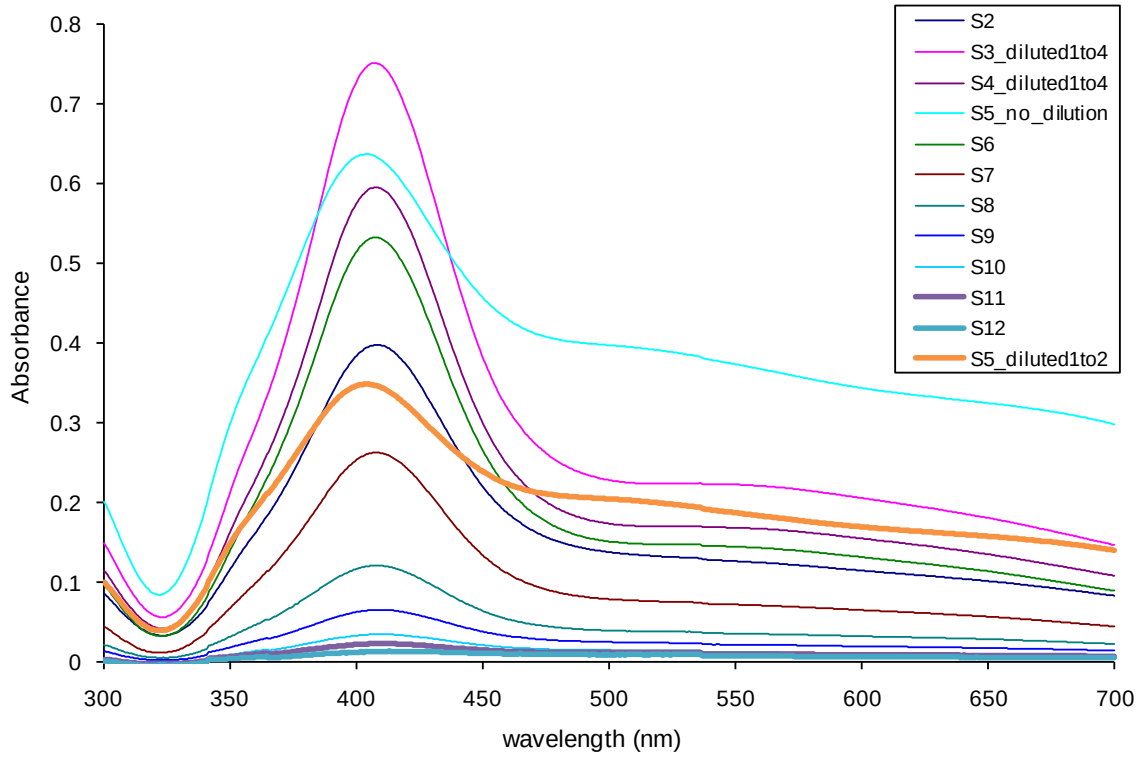

Figure 2.22: Absorbance of all effluent samples collected during silver nanoparticles injection experiment.

Most absorbance spectra have identical signature, except for sample S5 collected during the second post injected pore volume of water. Its spectrum was measured once at its original concentration and again after diluting it with two parts of pure water. Both

measurements (spectra) exhibited very similar signature but still different than the rest of the samples (Figure 2.22). Also note that samples (S3 and S4) collected during the second post injected pore volume were highly concentrated and therefore their absorbance spectra could not be measured directly. There were both diluted one part to four parts of pure water. The reported absorbance spectra (Figure 2.22) were for those diluted samples. The calibration curve was then used to obtain the corresponding concentrations for all samples (S2 to S12). Diluted samples (S3 and S4) concentration were calculated back using the following linear relationship.

$$C_1V_1 = C_2V_2 \tag{2.7}$$

where C_1 and C_2 are concentrations before and after dilution, respectively. V_1 and V_2 are sample volumes before and after dilutions, respectively.

Following the determination of the effluent samples concentration, the production history curve of the silver nanoparticles was estimated (Figure 2.23).

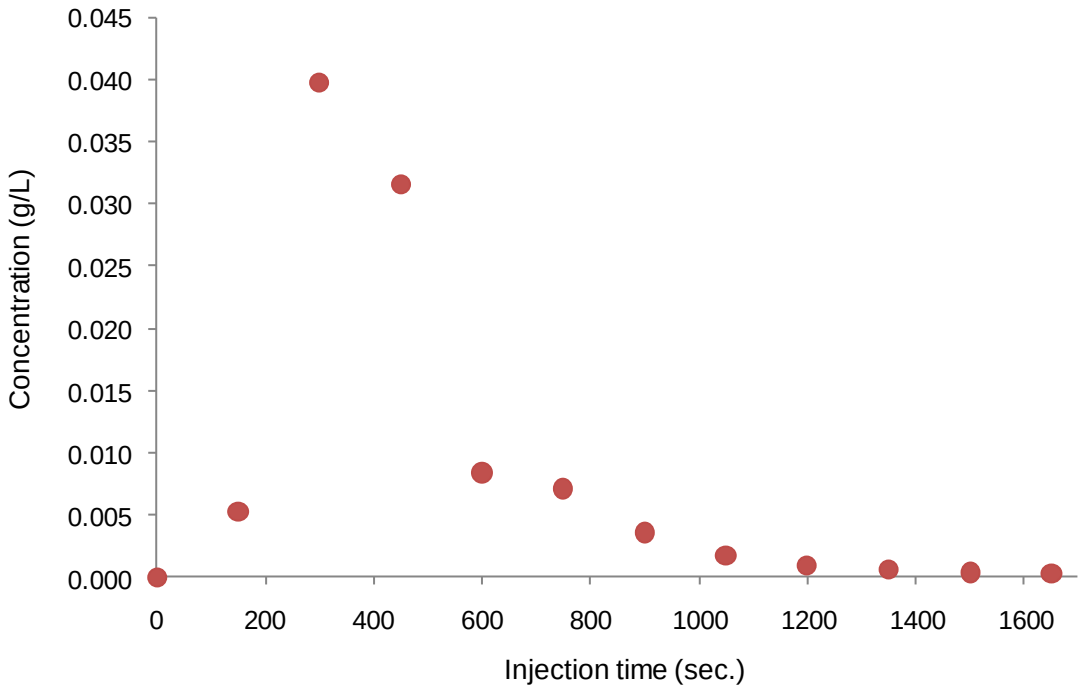

Figure 2.23: Production history (return curve) of silver nanoparticles.

The amount of nanoparticles recovered can be calculated by integrating the area under the return curve. A rough estimate has indicated that less than 25% of injected nanoparticles were recovered.

The final experiment to begin investigating the melting and cooling behavior of the Sn-Bi nanoparticles had inconclusive results due to the wide particle size distribution of the

original sample. The DLS results of the sample subjected to heating are shown in Figure 2.24.

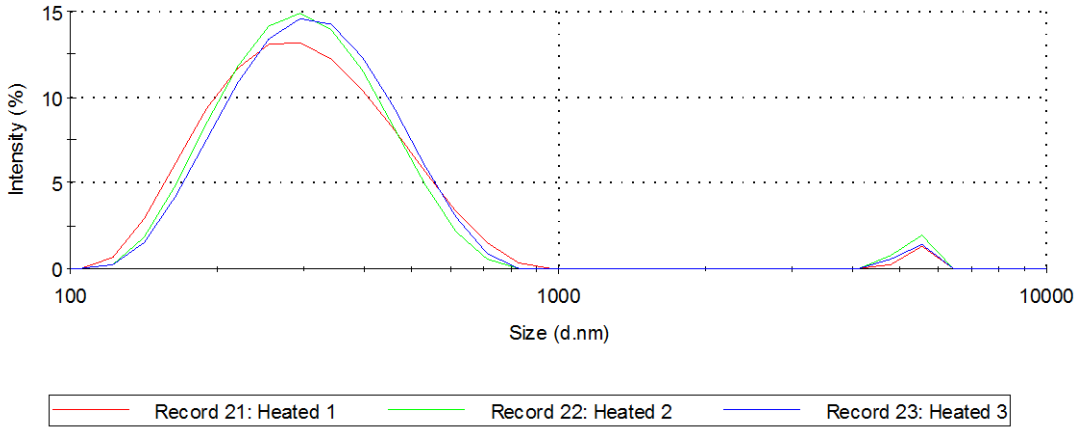

Figure 2.24: Logarithmic particle size distribution based on hydrodynamic diameter for heated Sn-Bi nanoparticle sample.

The three measurements are in relatively close agreement, with a standard deviation of about ±2 nm and an average modal value of 321 nm. The hydrodynamic diameter ranged from ~100 nm to ~1000 nm. Appreciable secondary peaks in the range of ~4100 nm to ~6400 nm are observed for all runs. This indicates that there are large particles in the sample, most likely do to aggregation and fusion of the particles during cooling. Selected particle size distribution curves for comparison of the original and heated samples are shown in Figure 2.25.

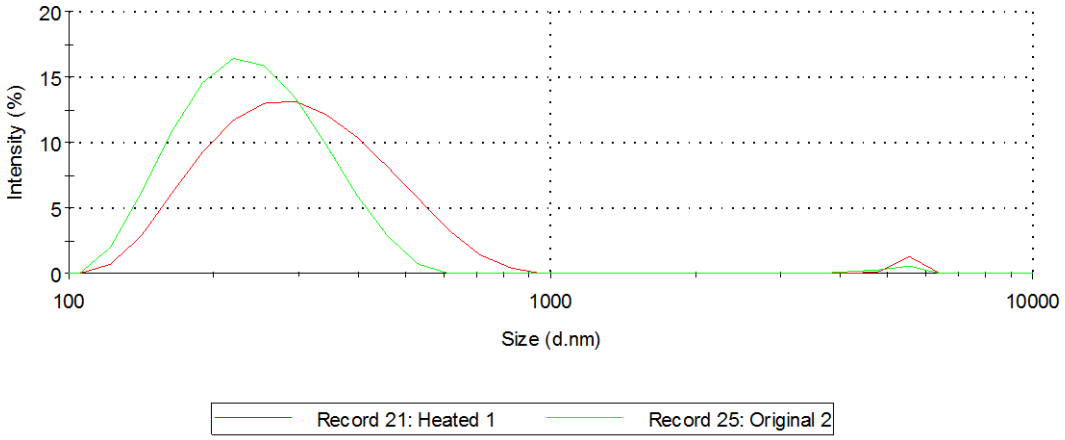

Figure 2.25: Comparison of logarithmic particle size distribution based on hydrodynamic diameter for original and heated Sn-Bi nanoparticle samples.

As shown in the figure, there is an appreciable difference in the particle size distribution upon heating, with a large standard deviation of ±61 nm. The heated sample has a wider distribution and exhibits larger particle sizes. Also, the second secondary peak in the

micron scale is noticeably larger, indicating that there are more large aggregates. SEM images of the heated sample are shown in Figures 2.26 and 2.27.

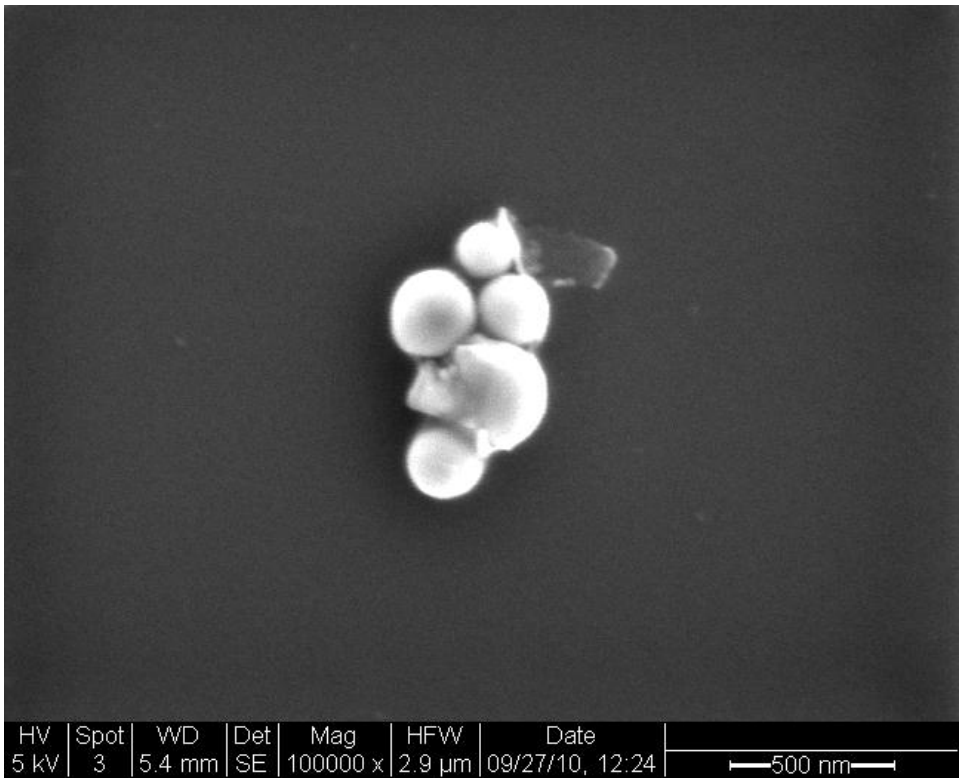

Figure 2.26: SEM image showing heated Sn-Bi nanoparticles.

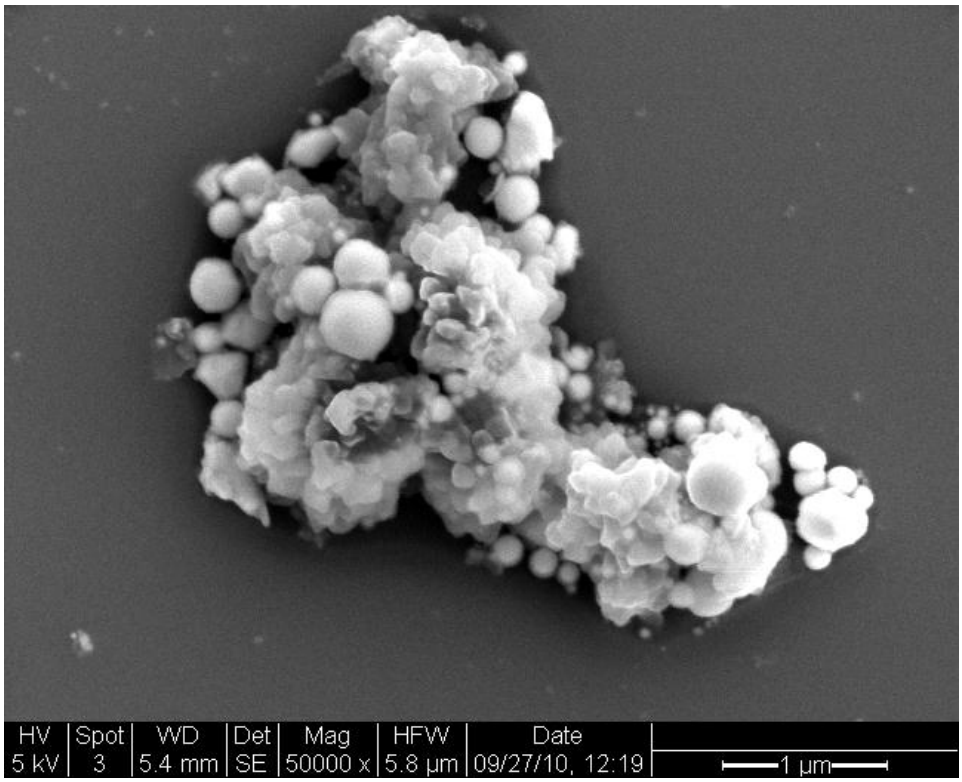

Figure 2.27: SEM image showing large aggregate of heated Sn-Bi nanoparticles.

Fusion of melted particles can be observed in both figures, and the sizes of both particles and large aggregates are within the range suggested by DLS results. While the fusion of melted particles could account for the shift in particle size distribution, it is difficult to come to any definite conclusions from the SEM results due to the very wide particle size distributions of both the heated and unheated samples.

2.8 FUTURE WORK

The next stage will be to inject pure water into the Berea core at higher flow rate in attempt to displace mobile silver nanoparticles. Also, the core will be backflushed with pure water to try to remobilize nanoparticles that might have been trapped at the inlet. The effluent samples will be characterized using UV-visible spectrophotometry as well as scanning electron microscopy. In addition, the experimental data will be fitted to an appropriate one-dimensional advection-dispersion model. The Sn-Bi synthesis will be repeated at a higher ultrasonic power with the goal of obtaining a more monodisperse and uniform sample, and they will be subject to more investigation, including flow and heating experiments. Finally, more advanced sensitive particles will be synthesized.

3. FRACTURE CHARACTERIZATION USING RESISTIVITY

This research project is being conducted by Research Assistant Lilja Magnusdottir, Senior Research Engineer Kewen Li and Professor Roland Horne. The objective of this project is to investigate ways to use resistivity to infer fracture properties in geothermal reservoirs.

3.1 SUMMARY

The aim of this part of the project is to use resistivity measurements and modeling to characterize fracture properties in geothermal fields. The resistivity distribution in the field can be estimated by measuring potential differences between various points and the resistivity data can be used to infer fracture properties due to the large contrast in resistivity between water and rock.

A two-dimensional model has been made to calculate a potential field due to point sources of excitation. The model takes into account heterogeneity by solving the potential field for inhomogeneous resistivity. Fractures are modeled as areas with resistivity different from the rock, to investigate the changes in the potential field around them. The grid is rectangular and nonuniform so the fracture elements can be modeled smaller than the elements for the rest of the reservoir, in order to decrease the total number of elements.

The possibility of using conductive fluid to enhance the contrast between fracture and rock resistivity is being explored together with the use of conductive fluid with time-dependent resistivity measurements. A flow simulation has been performed where the distribution of a conductive tracer is observed. The tracer, which increases the conductivity of the fluid, is injected into the reservoir and a program that reads the flow simulation's output into the resistivity model has been made. The changes of the potential field at different time steps were then calculated as the tracer transfers through the fractures in the reservoir. Those time-dependent changes in potential field as the conductive fluid flows through the fracture network facilitate fracture characterization.

3.2 INTRODUCTION

The designing of optimal production wells in geothermal reservoirs requires knowledge of the resource's connectivity and heat intensity for energy extraction. Drilling and construction of wells are expensive and the energy content from a well depends highly on the fractures it intersects. Fracture characterization is therefore important to increase the reliability of geothermal wells and thereby the overall productivity of geothermal power plants.

In this project, the goal is to find ways to use Electrical Resistivity Tomography (ERT) to characterize fractures in geothermal reservoirs. ERT is a technique for imaging the resistivity of a subsurface from electrical measurements. Typically, electrical current is injected into the subsurface through conducting electrodes and the resulting electrical potentials are measured. Due to the large contrast in resistivity between water and rock, the resistivity measurements could be efficiently used to indicate fracture locations.

Resistivity measurements have been used widely in the medical industry to image the internal conductivity of the human body, for example to monitor epilepsy, strokes and lung functions as discussed by Holder (2005). In Iceland, electrical resistivity tomography methods have been used to map geothermal reservoirs. Arnarson (2001) describes how different resistivity measurements have been used efficiently to locate high temperature fields by using electrodes located on the ground's surface. Stacey et al. (2006) investigated the feasibility of using resistivity to measure saturation in geothermal cores. A direct-current pulse was applied through electrodes attached in rings around a sandstone core and it resulted in data that could be used to infer the resistivity distribution and thereby the saturation distribution in the core. It was also concluded by Wang (2000) that resistivity data has high resolution power in the depth direction and is capable of sensing the areal heterogeneity.

In the approach considered in this project, electrodes would be placed inside geothermal wells and the resistivity anomalies between them studied to locate fractures and infer their properties by resistivity modeling. Due to the lack of measurement points, i.e. limited number of test wells, we will endeavor to find ways to ease the process of characterizing fractures from limited resistivity data. To enhance the contrast in resistivity between the rock and fracture zones, the possibility of using conductive fluid is being explored. Furthermore, the influences of temperatures and fluid stream on resistivity measurements will be studied. The effects of mineralization in the fractures will also be examined, because fractures containing a lot of minerals can be more difficult to distinguish from the surrounding rocks. This report first describes the resistivity model that has been made to calculate a potential field due to point sources of excitation and then discusses a flow simulation made to study how a conductive tracer distributes through a simple fracture network. The potential difference between the injection well and the production well is measured at each time step, to see whether the resulting graph can be used to infer the fracture properties.

3.3 RESISTIVITY MODELING

One of the main problems in resistivity modeling is to solve the Poisson's equation that describes the potential field and to efficiently complete the inversion iteration. That governing equation can be derived from some basic electrical relationships as described by Dey and Morrison (1979). Ohm's Law defines the relationship between current density, J, conductivity of the medium, σ, and the electric field, E, as:

$$J = \sigma E \tag{3.1}$$

The stationary electric fields are conservative, so the electric field at a point is equal to the negative gradient of the electric potential there, i.e.

$$E = -\nabla \phi \tag{3.2}$$

where ϕ is the scalar field representing the electric potential at the given point. Hence,

$$J = -\sigma \nabla \phi \tag{3.3}$$

Current density is the movement of charge density, so according to the continuity equation, the divergence of the current density is equal to the rate of change of charge density,

$$\nabla J = \frac{\partial Q(x,y,z)}{\partial t} = q(x,y,z) \tag{3.4}$$

where q is the current density in amp m^{-3}. Combining equations (3.3) and (3.4) gives the following Poisson's equation which describes the potential distribution due to a point source of excitation,

$$\nabla[\sigma \nabla \phi] = -q(x,y,z) \tag{3.5}$$

The conductivity σ is in mhos m^{-1} and the electric potential is in volts. This partial differential equation can then be solved numerically for the resistivity problem.

3.3.1 Finite Difference Equations in Two Dimensions

The finite difference method has been used to approximate the solution to the partial differential equation (3.5) using a point-discretization of the subsurface (Mufti, 1976). The computational domain was discretized into $Nx \times Ny$ blocks and the distance between two adjacent points on each block is *h* in the x-direction and *l* in the y-direction, as shown in Figure 3.1.

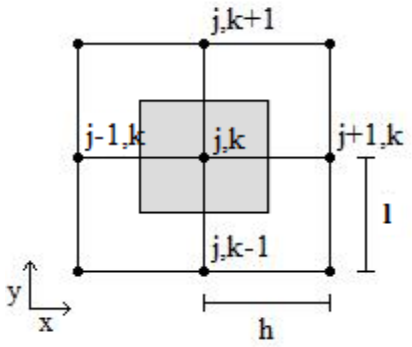

Figure 3.1: Computational domain, discretized into blocks.

Taylor series expansion is used to approximate the derivatives of Equation (3.5) about a point (*j*, *k*) on the grid,

$$\left.\frac{\partial}{\partial x}\left(\sigma \frac{\partial \phi}{\partial x}\right)\right|_{(j,k)} \approx \frac{\left[\begin{array}{l}\phi(j+1,k)\sigma\left(j+\frac{1}{2},k\right)+\phi(j-1,k)\sigma\left(j-\frac{1}{2},k\right)\\ -\left[\sigma\left(j+\frac{1}{2},k\right)\sigma\left(j-\frac{1}{2},k\right)\right]\phi(j,k)\end{array}\right]}{h^2} \tag{3.6}$$

$$\left.\frac{\partial}{\partial y}\left(\sigma \frac{\partial \phi}{\partial y}\right)\right|_{(j,k)} \approx \frac{\left[\begin{array}{l}\phi(j,k+1)\sigma\left(j,k+\frac{1}{2}\right)+\phi(j,k-1)\sigma\left(j,k-\frac{1}{2}\right)\\ -\left[\sigma\left(j,k+\frac{1}{2}\right)\sigma\left(j,k-\frac{1}{2}\right)\right]\phi(j,k)\end{array}\right]}{l^2} \tag{3.7}$$

The point (*j*, *k*) represents the shaded area in figure 3.1 (area = *hl*) so the current density due to an electrode at that point is given by,

$$q(j,k) = \frac{I}{hl} \tag{3.8}$$

where I [amp] is the current injected at point (j, k) Combining equations (3.5)-(3.8) and solving for the electric potential ϕ at point (j, k) gives,

$$\phi(j,k) = \frac{\left[Ihl + \phi(j+1,k)c_1 l^2 + \phi(j-1,k)c_2 l^2 + \phi(j,k+1)c_3 h^2 + \phi(j,k-1)c_4 h^2\right]}{\left[c_1 + c_2\right]l^2 + \left[c_3 + c_4\right]h^2} \tag{3.9}$$

The parameters c_i represent the conductivity averaged between two adjacent blocks, i.e.

$$c_1 = \frac{2}{\rho(j,k) + \rho(j+1,k)} \tag{3.10}$$

$$c_2 = \frac{2}{\rho(j,k) + \rho(j-1,k)} \tag{3.11}$$

$$c_3 = \frac{2}{\rho(j,k) + \rho(j,k+1)} \tag{3.12}$$

$$c_4 = \frac{2}{\rho(j,k) + \rho(j,k-1)} \tag{3.13}$$

where ρ(j, k) is the resistivity [ohm-m] of the node at grid coordinates j, k.

3.3.2 Iteration method

In order to solve Equation (3.9) numerically and determine the results for electrical potential ϕ at each point on the grid, an iteration method called Successive Over-Relaxation (SOR) was used (Spencer and Ware, 2009). At first, a guess is made for ϕ(j, k) across the whole grid, for example ϕ(j, k)= for all j, k. That guess is then used to calculate the right hand side of Equation (3.9) for each point and the new set of values for ϕ(j, k) is calculated using the following iteration scheme,

$$\phi_{n+1} = \omega Rhs + (1-\omega)\phi_n \tag{3.14}$$

The multiplier ω is used to shift the eigenvalues so the iteration converges better than simple relaxation. The number ω is between 1 and 2, and when the computing region is rectangular the following equation can be used to get a reasonable good value for ω,

$$\omega = \frac{2}{1 + \sqrt{1 - R^2}} \tag{3.15}$$

where:

$$R = \frac{\left(\cos\left(\frac{\pi}{Nx}\right) + \cos\left(\frac{\pi}{Ny}\right)\right)}{2} \tag{3.16}$$

The natural Neumann boundary condition is used on the outer boundaries in this project, i.e. $\frac{\partial \phi}{\partial n} = 0$.

3.4 RESULTS

First, a flow simulation was performed using TOUGH2 reservoir simulator to see how a tracer, which increases the conductivity of the fluid, distributes after being injected into the reservoir. The simulation was carried out on a two-dimensional grid with dimensions $1000\times1000\times10$ m^3. The fracture network can be seen in Figure 3.2, where the green blocks represent the fractures and wells are located at the upper left and lower right corner of the network.

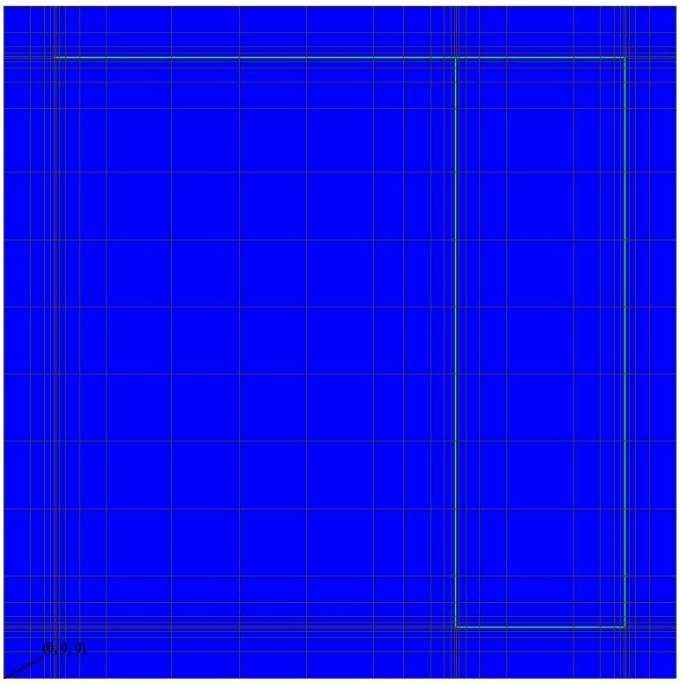

Figure 3.2: Fracture network.

The fracture blocks were given a porosity value of 0.65 and permeability value of 5×10^{11} md (5×10^{-4} m^2) and the rest of the blocks were set to porosity 0.1 and permeability 1 md (10^{-15} m^2). Closed or no-flow boundary conditions were used and one injector at upper left corner, at (76, 924) m, was modeled to inject water at 100 kg/sec with enthalpy 100 kJ/kg, and a tracer at 0.01 kg/s with enthalpy 100 kJ/kg. One production well at lower right corner, at (924, 76) m, was configured to produce at 100 kg/s.

The initial pressure was set to 10.13 MPa (100.13 bar), temperature to 150°C and initial tracer mass fraction was set to 10^{-9} because the simulator could not solve the problem with zero initial tracer mass fraction. Figure 3.3 illustrates how the tracer transfered through the fractures from the injector to the producer. After 4 days the tracer had distributed through the whole fracture network.

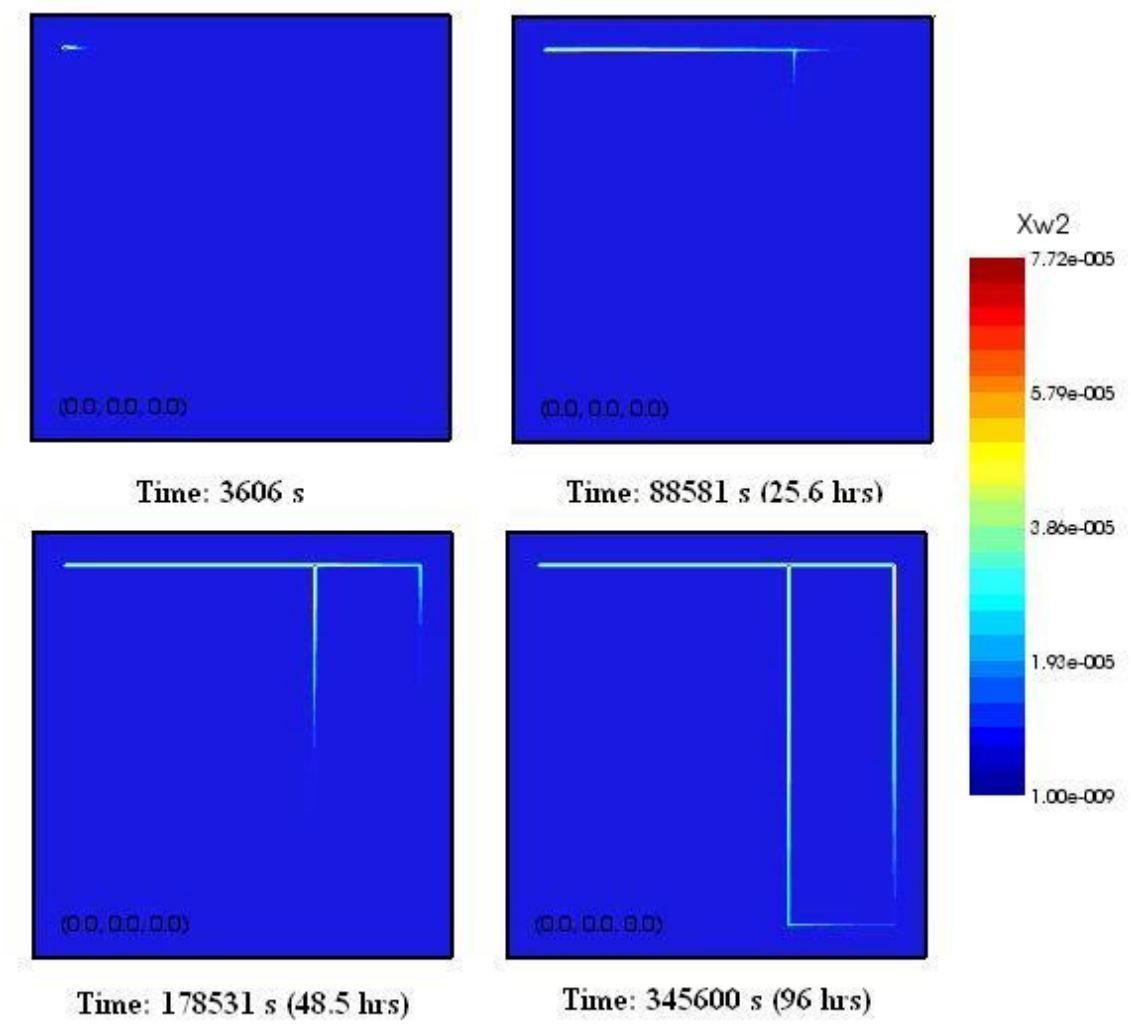

Figure 3.3: Flow simulation's results for tracer concentration.

The resistivity model was changed so it had the same grid as the flow model and a program was made to read the results from the flow simulation and write them into the resistivity model, so that the right conductivity values can be assigned for the reservoir. The conductivity value of each block depends on the tracer concentration in that block, and it was assumed that the tracer decreases the conductivity, like for example a saline tracer. Table 1 shows how the conductivity values were assigned to different tracer concentration, X_2.

Table 3.1: Tracer concentration and corresponding conductivity values.

Tracer concentration	Conductivity $[(\text{ohm-m})^{-1}]$
$X_2 \leq 1 \cdot 10^{-9}$	2.4
$10^{-9} < X_2 \leq 10^{-8}$	15
$10^{-8} < X_2 \leq 10^{-7}$	20
$10^{-7} < X_2 \leq 10^{-6}$	25

$10^{-6} < X_2 \leq 10^{-5}$	30
$X_2 \geq 10^{-5}$	35

The flow simulation calculated the tracer concentration at 97 different time steps and for each step the potential field was calculated using the resistivity model. Figure 3.4 shows the potential field for the four time steps shown in Figure 3.3.

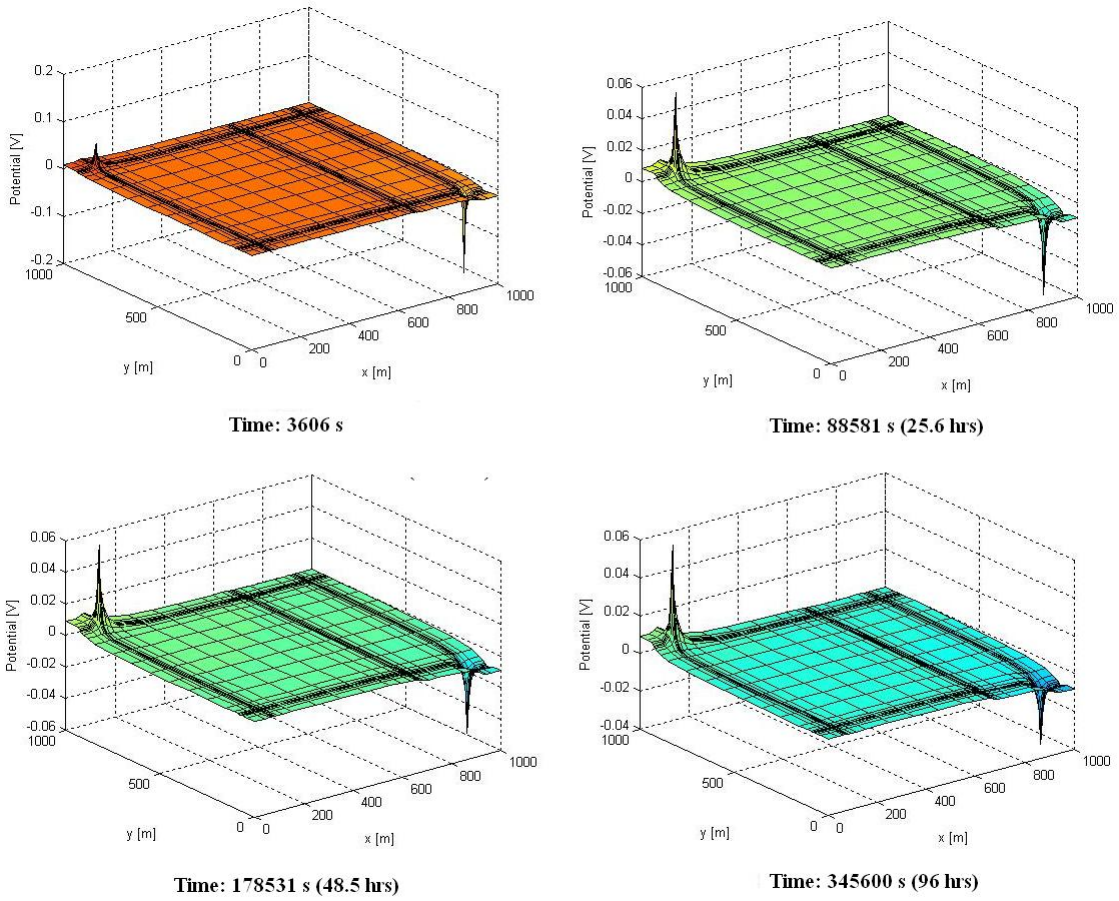

Figure 3.4: Flow Potential field at four different time steps.

First, the tracer had only started flowing through the fracture from the injection well, but not reached the production well or the main fracture between them, so the potential difference was large. The potential was larger at the production well, because it distributed over a larger area near the injection well due to the tracer. Next, the tracer had gone through the middle fracture, which decreased the potential difference enormously. After that the tracer kept flowing through the fractures, but the change in the potential difference was much less.

The potential difference between the injection well and the production well at each time step is shown in Figure 3.5.

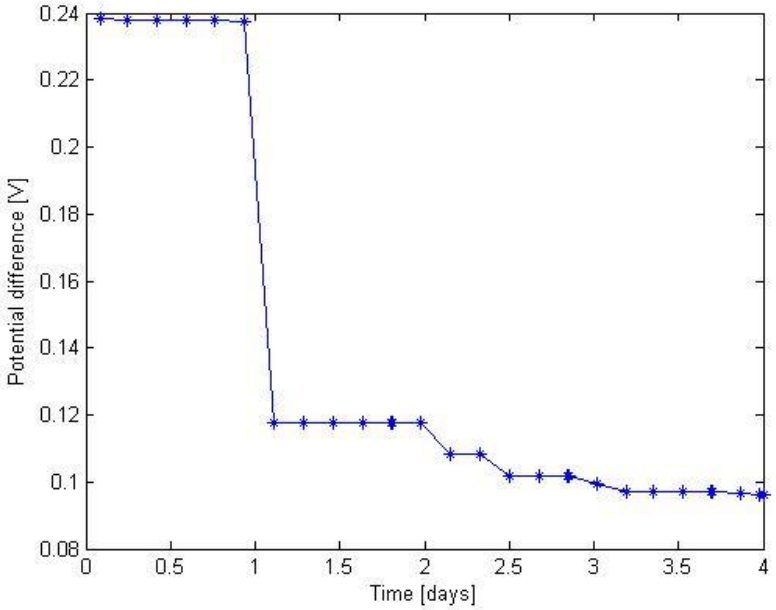

Figure 3.5: Potential difference between two wells at different time steps.

The potential difference between the wells decreases as more of the conductive tracer is injected into the reservoir. The difference changes dramatically between 0.938 days and 1.112 days, but at 1.112 days the whole middle fracture receives a tracer concentration of more than 10^{-9}. Another jump can be seen in the potential difference after approximately two days, but at that time the whole fracture network receives a tracer concentration of more than 10^{-9}. The graph of the potential differences corresponds in that way to the fracture network, so by measuring the potential differences between two wells while injecting conductive tracer, some information about the network can be gained.

3.5 FUTURE WORK

One of the next steps is to calculate the time-dependent potential difference, while injecting conductive tracer, for different fracture patterns to study the correspondence between the potential difference and the fracture network. Other future goals are to use inverse modeling to estimate the fracture network from the potential difference measured between the wells. The initial study will use data from many wells at different locations, but then the number of wells will be decreased to see if it is possible to infer the fracture properties using only a few wells.

The influences of temperatures on water resistivity as well as the potential changes due to fluid stream in the fractures will also be studied. The effects of mineralization will be examined as well since it could be difficult to distinguish resistivity between rock and fractures containing a lot of minerals.

4. REFERENCES

Amyx, J. W., Bass, D. M. Jr., and Whiting, R. L. (1960), Petroleum Reservoir Engineering, Physical Properties. McGraw-Hill Book Co.

Arnason, K.: Viðnámsmælingar í Jarðhitarannsóknum á Íslandi, Orkustofnun, Orkuþing (2001).

Barker, J.: A generalized radial flow model for hydraulic tests in fractured rock. Water Resources Research, (1988).

Breiman, L., and Friedman, J. H.: Estimating optimal transformations for multiple regression and correlation. Journal of the American Statistical Association, 80(391), 580–598, (1985).

Carlier, E.: Analytical solutions of the advection-dispersion equation for transient groundwater flow. A numerical validation. Hydrological Processes, (2008).

Chen, Hongjie, Li, Zhiwei, Wu, Zhishen and Zhang, Zhijun: "A novel route to prepare and characterize Sn-Bi nanoparticles," Journal of Alloys and Compounds. 2005, 394, 282-285.

Deng, X., and Horne, R.: Well Test Analysis of Heterogeneous Reservoirs. SPE Annual Technical Conference and Exibition, Houston, Texas, (1993).

Dey, A. and Morrison, H.F.: Resistivity Modelling for Arbitararily Shaped Two-Dimensional Structures, Geophysical Prospecting 27, I06-I36, University of California, Berkeley, CA (1979).

Digital image. Phase Diagrams & Computational Thermodynamics. The National Institute of Standards and Technology. Web. 7 July 2010. <http://www.metallurgy.nist.gov/phase/solder/bisn.html>.

Holder, D.S.: Electrical Impedance Tomography: Methods, History and Applications, IOP, UK (2004).

Horne, R. N., and Szucs, P.: Inferring Well-to-Well Connectivity Using Nonparametric Regression on Well Histories. Proceedings, Thirty-Second Workshop on Geothermal Reservoir Engineering, Stanford University, Stanford, California, (2007).

Jensen, C., and Horne, R.: Matrix diffusion and its effect on the modeling of tracer returns from the fractured geothermal reservoir at Wairakei, New Zealand. Proc. Ninth Workshop on Geothermal Reservoir Engineering, Stanford University, Stanford, California, (1983).

Kanj, M., Funk, J., and Al-Yousif, Z.: "Nanofluid Coreflood Experiments in the Arab-D," SPE paper 126161, presented at the 2009 SPE Saudi Arabia Technical Symposium and Exhibition held in Saudi Arabia, Alkhobar, May 09-11.

Kim, D., Jeong, S. and Moon, J.: " Synthesis of sliver nanoparticles using the polyol process and the influence of precursor injection," Nanotechnology 17 (2006), 4019-4024

Lee, K. H., Ortega, A., Jafroodi, N., and Ershaghi, I. (2010). A Multivariate Autoregressive Model for Characterizing Producer Producer Relationships in Waterfloods from Injection/Production Rate Fluctuations,

Lee, K. H., Ortega, Antonio, Nejad, A., Jafroodi, Nelia, and Ershaghi, Iraj.: A Novel Method for Mapping Fractures and High Permeability Channels in Waterfloods Using Injection and Production Rates. Proceedings of SPE Western Regional Meeting. Society of Petroleum Engineers (2009).

Lee, W. J.: Well testing. Society of Petroleum Engineers. (1982).

Levard, Clement. <clevard@stanford.edu (2010, July 8)>. [Personal email].

Levitan, M.: Practical Application of Pressure/Rate Deconvolution to Analysis of Real Well Tests. SPE Reservoir Evaluation and Engineering, (2005), 8 (2): 113–121,

Levitan, M.: Deconvolution of multiwell test data. SPE Annual Technical Conference and Exhibition, (2006), 24-27.

Mufti, I.R.: Finite-Difference Resistivity Modeling for Arbitrarily Shaped Two-Dimensional Structures, Geophysics, 41, (1976), 62-78.

Nomura, M., and Horne, R.: Data processing and interpretation of well test data as a nonparametric regression problem. SPE Western Regional Meeting (2009).

Onur, M., Ayan, C., and Kuchuk, F.: Pressure-Pressure Deconvolution Analysis of Multiwell Interference and Interval Pressure Transient Tests. Proceedings of International Petroleum Technology Conference. Society of Petroleum Engineers, (2009).

Pimonov, E., Ayan, C., Onur, M., and Kuchuk, F.: A New Pressure Rate Deconvolution Algorithm to Analyze Wireline Formation Tester and Well-Test Data. Proceedings of SPE Annual Technical Conference and Exhibition, (2009), 1-23.

Sayarpour, M., Zuluaga, E., Kabir, C. S., and Lake, L. W. The Use of Capacitance-Resistive Models for Rapid Estimation of Waterflood Performance and Optimization. SPE Annual Technical Conference and Exhibition. Society of Petroleum Engineers, (2006).

Schroeter, T. von, Hollaender, F., and Gringarten, A. C.: Deconvolution of Well-Test Data as a Nonlinear Total Least-Squares Problem. SPE Journal, 9(4), (2004).

Schroeter, T. v., and Gringarten, A.: Superposition Principle and Reciprocity for Pressure-Rate Deconvolution of Data From Interfering Wells. SPE Annual Technical Conference, (2007).

Spencer, R.L. and Ware, M.: Computational Physics 430, Partial Differential Equations, Department of Physics and Astronomy, Brigham Young University (2009).

Sullera, M. M., and Horne, R. N.: Inferring injection returns from chloride monitoring data. Geothermics, (2001), 30(6), 591–616. Elsevier.

Stacey, R.W., Li, K. and Horne, R.N.: Electrical Impedance Tomography (EIT) Method for Saturation Determination, Proceedings, 31st Workshop on Geothermal Reservoir Engineering, Stanford University, Stanford, CA (2006).

The MathWorks: Partial Differential Equation Toolbox 1, The MathWorksTM, Inc. (2003).

Urbino, E. G., and Horne, R. N.: Optimizing reinjection strategy at Palinpinon, Philippines, based on chloride data. Sixteenth Workshop on Geothermal Reservoir Engineering. Stanford: Stanford University, (1991).

Wang, P. and Horne, R.N.: Integrating Resistivity Data with Production Data for Improved Reservoir Modelling, SPE 59425, SPE Asia Pacific Conference, Yokohama, Japan (2000).

Wittung, P., Kajanus, J., Kubista, M., and Malmström, Bo G. (1994). "Absorption flattening in the optical spectra of liposome-entrapped substances," FEBS Letter 352, 37-40.

Yousef, A., Gentil, P., Jensen, J., and Lake, L.: A capacitance model to infer interwell connectivity from production and injection rate fluctuations. SPE Reservoir Evaluation & Engineering. (2005).

Zuber, A.: Theoretical possibilities of the two-well pulse method, Symposium on isotope techniques in groundwater hydrology, Vienna, Austria, (1974).